

# JGR Atmospheres

## RESEARCH ARTICLE

10.1029/2018JD030009

### Key Points:

- Aerosol properties are obtained using a novel synergistic retrieval of in situ angular-dependent scattering and absorption measurements
- Biomass burning particles were found to have elevated real and imaginary refractive indices relative to other aerosol types
- Significant concentrations of dust-like particles are observed in measurements made in the vicinity of convective systems

### Supporting Information:

- Figure S1

### Correspondence to:

W. R. Espinosa,  
 reedespinosa@umbc.edu

### Citation:

Espinosa, W. R., Vanderlei Martins, J., Remer, L. A., Dubovik, O., Lapyonok, T., Fuertes, D., et al. (2019). Retrievals of aerosol size distribution, spherical fraction, and complex refractive index from airborne in situ angular light scattering and absorption measurements. *Journal of Geophysical Research: Atmospheres*, 124, 7997–8024. <https://doi.org/10.1029/2018JD030009>

Received 16 NOV 2018

Accepted 1 JUN 2019

Accepted article online 13 JUN 2019

Published online 29 JUL 2019

### Author Contributions

**Conceptualization:** W. Reed







Espinosa, J. Vanderlei Martins, Oleg Dubovik

**Data curation:** W. Reed Espinosa

**Funding Acquisition:** W. Reed Espinosa, J. Vanderlei Martins, Daniel Orozco, Luke Ziemba, K. Lee Thornhill, Robert Levy

**Methodology:** W. Reed Espinosa, J. Vanderlei Martins, Lorraine A. Remer, Oleg Dubovik, Anin Puthukkudy, Daniel Orozco, Luke Ziemba, K. Lee Thornhill, Robert Levy

## Retrievals of Aerosol Size Distribution, Spherical Fraction, and Complex Refractive Index From Airborne In Situ Angular Light Scattering and Absorption Measurements

W. Reed Espinosa<sup>1,2</sup> , J. Vanderlei Martins<sup>2,3</sup>, Lorraine A. Remer<sup>2,3</sup>, Oleg Dubovik<sup>4</sup>, Tatyana Lapyonok<sup>4</sup>, David Fuertes<sup>5</sup>, Anin Puthukkudy<sup>2,3</sup> , Daniel Orozco<sup>2,3</sup> , Luke Ziemba<sup>6</sup> , K. Lee Thornhill<sup>6</sup> , and Robert Levy<sup>1</sup> 

<sup>1</sup>NASA Goddard Space Flight Center, Greenbelt, MD, USA, <sup>2</sup>Department of Physics, University of Maryland, Baltimore County, Baltimore, MD, USA, <sup>3</sup>Joint Center for Earth Systems Technology, Baltimore, MD, USA, <sup>4</sup>Laboratoire d'Optique Atmosphérique, UMR8518, CNRS - Université de Lille 1, Villeneuve d'Ascq, France, <sup>5</sup>GRASP-SAS, Bat-P5, Université de Lille 1, Villeneuve d'Ascq, France, <sup>6</sup>NASA Langley Research Center, Hampton VA, USA

**Abstract** Aerosol models, composed of size distribution, complex refractive index, and spherical fraction, are derived from a new synergistic retrieval of airborne in situ angular scattering measurements made by the Polarized Imaging Nephelometer and absorption measurements from the Particle Soot Absorption Photometer. The data utilized include phase function ( $F_{11}$ ), degree of polarization ( $-F_{12}/F_{11}$ ), and absorption coefficient ( $\beta_{abs}$ ) measured at low relative humidities during the Studies of Emissions and Atmospheric Composition, Clouds, and Climate Coupling by Regional Surveys (SEAC<sup>4</sup>RS) and Deep Convection Clouds and Chemistry (DC3) field campaigns. The Generalized Retrieval of Aerosol and Surface Properties (GRASP) is applied to these measurements to obtain summaries of particle properties that are optically consistent with the original measurements. A classification scheme is then used to categorize the corresponding retrieval results. Inversions performed on the DC3 measurements indicate the presence of a significant amount of dust-like aerosol in the inflow of storms sampled during this campaign, with the quantity of dust present depending strongly on the underlying surface features. In the SEAC<sup>4</sup>RS data, the retrieved size distributions were found to be remarkably similar among a range of aerosol types, including urban and industrial, biogenic, and biomass burning (BB) emissions. These aerosol types were found to have average fine mode volume median radii  $0.155 \leq r_{vf} \leq 0.163 \mu\text{m}$  and lognormal standard deviations  $0.32 \leq \sigma_f \leq 0.36$ . There were, however, consistent differences between the angular scattering patterns of the BB samples and the other particle types. The GRASP retrieval predominantly attributed these differences to elevated real and imaginary refractive indices in the BB samples ( $m_{532nm} \approx 1.55 + 0.007i$ ) relative to the two other categories ( $m_{532nm} \approx 1.51 + 0.004i$ ).

## 1. Introduction

Identifying, quantifying, and monitoring atmospheric particulates, called aerosols, at global scales has become essential for a variety of critical applications. Aerosols affect Earth's energy balance, and therefore climate, directly through the scattering and absorption of light (Bellouin et al., 2005) and indirectly by influencing cloud properties (Rosenfeld et al., 2008). However, the magnitudes of both of these effects are not well constrained (Stocker, 2014). Furthermore, these particles adversely affect air quality, becoming a serious threat to global public health (Gakidou et al., 2017). Local ground-based particulate monitoring sites meet some of this need but cannot provide the global context of satellite measurements (Wang & Christopher, 2003). Space-based remote sensing instrumentation yield aerosol data with global coverage but are dependent on assumptions of particle properties in order to translate satellite-measured radiance into quantitative aerosol loading or mass (Tanré et al., 1997; Van Donkelaar et al., 2006). These assumptions commonly take the form of sets of predefined particle properties, called “aerosol models,” that are linked to specific aerosol types (e.g., desert dust, biomass burning [BB], and urban emissions). If an aerosol model is to facilitate the simulation of radiation in the atmosphere, it must contain a sufficiently comprehensive set of parameters to

**Software:** W. Reed Espinosa, Oleg Dubovik, Tatyana Lapyonok, David Fuertes, Anin Puthukkudy, Luke Ziemba, K. Lee Thornhill, Robert Levy

**Writing - Original Draft:** W. Reed Espinosa, Lorraine A. Remer

**Formal Analysis:** Oleg Dubovik, Tatyana Lapyonok, Luke Ziemba, K. Lee Thornhill

**Investigation:** W. Reed Espinosa, David Fuertes, Anin Puthukkudy, Daniel Orozco, Luke Ziemba, K. Lee Thornhill, Robert Levy

**Project Administration:** J. Vanderlei Martins

**Supervision:** J. Vanderlei Martins, Daniel Orozco, Luke Ziemba, K. Lee Thornhill, Robert Levy

**Visualization:** W. Reed Espinosa

**Writing - review & editing:** Lorraine A. Remer, Oleg Dubovik, Anin Puthukkudy, Daniel Orozco, Luke Ziemba, K. Lee Thornhill, Robert Levy

reproduce the bulk optical properties of the constituent particles. This set of parameters is often expressed in terms of the particle size distribution (PSD), complex refractive index ( $m = n + ik$ ), and a set of assumptions regarding particle morphology. While current algorithms are adequate to retrieve aerosol optical depth (AOD) and a few other parameters, the results from a wide range of studies have suggested that there is still room for significant improvements in the aerosol properties assumed in space-based remote sensing retrievals (Bilal et al., 2013; Lee et al., 2012; Wong et al., 2011). Moreover, comparisons of widely used aerosol forcing models have shown that the largest source of diversity in model estimates of forcing does not result from the models' representation of aerosol loading, but instead from deviations in the intensive properties of the particles (Myhre et al., 2013; Schulz et al., 2006). Thus, the key to improvement of the global representation of aerosols, aerosol radiative effects, estimated climate change, and public health rests on better representation of aerosol particle properties or aerosol models in both remote sensing algorithms and global climate models.

Currently, the satellite remote sensing community primarily depends on retrieved properties from the ground-based sun/sky scanning radiometers composing the Aerosol Robotic Network (AERONET; Holben et al., 1998) for their aerosol models, especially at visible and near-infrared wavelengths (Dubovik et al., 2002; Levy et al., 2007). The ground-based nature of these instruments allows them to make extended observations of aerosols with minimal influence from the underlying surface, permitting accurate aerosol retrievals, without the need for the strong a priori assumptions frequently required by space-based sensors. AERONET enjoys a long data record and a broad geographical distribution, creating the statistics necessary to cover a wide range of global aerosol types. Moreover, AERONET retrievals return aerosol optical properties representative of the total atmospheric column under ambient conditions, which is key for remote sensing from imaging sensors and important for constraining climate models. However, as a single technique AERONET also contains limitations and biases. In order for AERONET to produce the high-accuracy retrieval required to develop a complete aerosol model a range of conditions must be met including high aerosol loading ( $AOD_{440nm} > 0.4$ ), appropriate solar geometry, and a virtually cloud free sky. In the derivation of the current aerosol models, implemented in the operational retrievals of the widely used Moderate Resolution Imaging Spectroradiometers, only 14% of AERONET observations met the required criteria (Levy et al., 2007). Additionally, geometric constraints prohibit AERONET almucantar scans from sampling scattering angles larger than  $150^\circ$  (Schafer et al., 2014). As a result of this limitation, AERONET-derived aerosol models can not guarantee optical consistency at the highest scattering angles, a region that is frequently sampled by space-based remote sensors.

While in situ measurements have their own set of limitations, their unique strengths have the potential to complement the shortcomings of other techniques. For example, in situ measurements can maintain reasonable accuracy down to relatively low aerosol concentrations and are made independent of solar geometry. Furthermore, in situ data have the potential to provide additional information, such as aerosol vertical dependence and particle hygroscopicity, while maintaining an optical consistency comparable to remote sensors. In practice, though, the majority of in situ optical measurements have been limited to parameters, such as total scattering, absorption, and extinction, which lack the angular information required for a comprehensive aerosol model that is optically consistent with directional remote sensing measurements made from satellites.

Recently, a new in situ instrument, the Polarized Imaging Nephelometer (PI-Neph; Dolgos & Martins, 2014), was introduced to measure aerosol particle scattering, as a function of angle, from an airborne platform. Measuring two elements of the scattering matrix, phase function ( $F_{11}$ ) and degree of linear polarization ( $-F_{12}/F_{11}$ ) over a wide angular range, enabled robust distinction between aerosol types from the scattering measurements alone (Espinosa et al., 2018). Applying the Generalized Retrieval of Aerosol and Surface Properties (GRASP; <http://www.grasp-open.com>; Dubovik et al., 2014) to these measurements with minimal assumptions demonstrated that such parameters as PSD and the real part of the refractive index could be obtained with at least the same accuracy as most standard in situ techniques (Espinosa et al., 2017). Although polar nephelometers, such as the PI-Neph, are not new, the ability to fly the PI-Neph through a variety of different aerosol types of suspended particles above the immediate surface layer is unprecedented. The accumulation of thousands of samples from the PI-Neph and the ability to apply inversion software to retrieve size distribution and the refractive index presents an opportunity to create a set of aerosol models representative of the aerosol types encountered during the PI-Neph's deployments over the contiguous United States. Furthermore, the PI-Neph can sample at aerosol scattering intensities as low

as  $10 \text{ Mm}^{-1}$ , permitting retrievals in many cases where AERONET lacks sufficient sensitivity. For example, a 2.5-km-thick layer of nonabsorbing aerosol would require a mean scattering coefficient of  $160 \text{ Mm}^{-1}$  to reach the  $AOD_{440nm} > 0.4$  threshold required for AERONET to produce level 2 inversions of refractive index or single scattering albedo. The objective of this study is to go beyond a demonstration and use the techniques developed previously (Espinosa et al., 2017, 2018) to provide aerosol models of the types of aerosols encountered by the PI-Neph on its major deployments.

A key parameter of an aerosol model is the spectral absorption properties of the particles, which are strongly linked to the imaginary part of the refractive index. The PI-Neph measures the angular dependence of the light scattered by the aerosol but does not directly measure particle absorption. An inversion procedure that makes use of angular scattering data measured over a wide angular range is able to partially constrain the absorption properties of an aerosol, but only to a rudimentary level. In this work, this limitation is overcome by incorporating a direct measurement of particle absorption, made in parallel to the PI-Neph, into the retrieval algorithm. To the authors' knowledge, this is the first time absorption measurements have been paired with angular scattering data in order to obtain complex refractive index. This additional constraint on absorption, provided by the Particle Soot Absorption Photometer (PSAP), is generally shown to significantly improve the accuracy of the imaginary refractive index without negatively affecting the other retrieved parameters.

In section 2 of this paper we will introduce the measurement techniques, data standardization procedures, and aerosol classification scheme to be used. Section 3 describes the retrieval approach, explores the consequences of incorporating PSAP data, and presents the results of a Monte Carlo simulation designed to estimate the uncertainties in the retrieved parameters. Once the inversion uncertainty has been determined, in section 4 we apply the procedure to the full record of appropriate PI-Neph data and produce a set of aerosol models with reported uncertainty for six different aerosol categories. Conclusions are presented in section 5.

## 2. Data

The retrievals in this work are performed on airborne measurements made by the PI-Neph and PSAP instruments during two recent field campaigns. Data from the two instruments, which both sampled from the Langley Aerosol Research Group Experiment's (LARGE) isokinetic inlet aboard the DC-8 aircraft, are averaged over coincident periods during which higher aerosol concentrations were observed. The resulting samples are then classified based on ancillary measurements of trace gasses, aerosol composition, aerodynamic particle size, and geographic location. These classification categories include dust, biogenic, urban, and BB particles as well as three categories of aerosol associated with convective systems. These data are then further averaged over all samples of a given classification to obtain a single set of measured optical properties representative of the aerosol type in question.

### 2.1. Airborne Measurement Techniques

The aerosol models derived in this work are retrieved from measurements made over the contiguous United States during the Deep Convection Clouds and Chemistry (DC3) and Studies of Emissions and Atmospheric Composition, Clouds, and Climate Coupling by Regional Surveys (SEAC<sup>4</sup>RS) field experiments. The DC3 campaign, which took place in the spring of 2012, was designed to improve the scientific community's understanding of storm dynamics and the effect of convective systems on the chemical composition of the troposphere (Barth et al., 2015). The majority of DC3 flights focused on one of three study regions: northeastern Colorado, northern Alabama, and a region comprising northern Texas and southern Oklahoma (Barth et al., 2015). In August of 2013 the associated SEAC<sup>4</sup>RS campaign began its 2-month-long deployment over the western and southeastern United States (SEUS). This campaign targeted a variety of atmospheric phenomena including convection's influence on the distribution of aerosols and gasses within the troposphere, the climatic and meteorological effects of BB, and anthropogenic emissions as well as the calibration and validation of satellite data (Toon et al., 2016). Multiple aircraft were involved in both campaigns, but the data used in this work come solely from measurements made aboard the NASA DC-8. This platform took part in over 20 flights in each campaign producing a combined total of almost 300 flight hours of data.

The retrieved properties presented here are derived primarily from phase function and degree of linear polarization measurements made by the PI-Neph at low relative humidities ( $RH < 40\%$ ). The PI-Neph uses a wide field of view imaging system to measure the angular dependence of light scattered by aerosols and the surrounding gasses (Dolgos & Martins, 2014). While the PI-Neph's fundamental design was similar in both the

DC3 and SEAC<sup>4</sup>RS campaigns, different physical builds of the instrument were used in the two experiments. In DC3 the PI-Neph utilized only one laser light source operating at 532 nm, but two additional lasers were incorporated into the second instrument flown in SEAC<sup>4</sup>RS, adding measurements at 473 and 671 nm. The incorporation of calibration data derived from molecular scatterers ( $\text{CO}_2$  and  $\text{N}_2$ ) that are well characterized (Anderson et al., 1996; Young, 1980) allows for an angular-dependent calibration that produces direct measurements of absolute phase function in known units (e.g.,  $\text{Mm}^{-1} \text{sr}^{-1}$ ), free from any angular truncation error. The angular range of the resulting measurements were typically  $4^\circ$  to  $174^\circ$  in SEAC<sup>4</sup>RS and  $5^\circ$  to  $170^\circ$  in DC3, with an angular resolution of  $1^\circ$ .

Absorption coefficient ( $\beta_{\text{abs}}$ ) measurements made by the PSAP (Radiance Research, Seattle, WA) were also input into the GRASP inversion, primarily to improve sensitivity to the retrieved imaginary refractive index. The absorption coefficient reported by PSAP is derived from changes in the transmission of a filter resulting from the deposition of particles on the filter's surface (Bond et al., 1999). A three-wavelength PSAP was used in this work with transmission measurements made at 470, 532, and 660 nm. The raw transmission measurements were corrected for a variety of artifacts including scattering, illumination spot size, and sample flow rate using the method of Virkkula (2010). A separate three-wavelength ( $\lambda = 450, 550, 700$  nm) integrating nephelometer (TSI Model 3563) was used to perform the PSAP scattering correction. The 700-nm channel of this nephelometer was not functioning during the SEAC<sup>4</sup>RS campaign, so the PSAP 660-nm data were not used in this work, as no reliable correction could be performed.

Ancillary data sets, which are independent of aerosol optical properties, are used in this study to classify the sampled air masses. In this work the Particle Analysis by Laser Mass Spectrometry (PALMS; Thomson et al., 2000) instrument is used to aid in the identification of aerosols containing significant amounts of mineral dust. Identification of dust aerosols is also aided by measurements made by the aerodynamic particle sizer (APS model 3321, TSI Inc., St. Paul, MN, USA), which measures particle time-of-flight inside an accelerating air flow. Trace gas concentrations are used to identify air masses corresponding to urban, biogenic, and BB emissions. Measurements of nitrogen dioxide ( $\text{NO}_2$ ) were made by National Oceanic and Atmospheric Administration's NOyO3 instrument using the UV-LED photolysis-chemiluminescence technique (Pollack et al., 2010; Ryerson et al., 2000). Carbon monoxide volume mixing ratios were obtained with the Differential Absorption Carbon Monoxide Monitor (Fried et al., 2008). The University of Innsbruck's High-Temperature Proton-Transfer-Reaction Mass Spectrometer (Mikoviny et al., 2010) was used to quantify the mixing ratio of the remaining gas species, specifically acetonitrile ( $\text{CH}_3\text{CN}$ ), isoprene ( $\text{C}_5\text{H}_8$ ), and monoterpenes ( $\text{C}_{10}\text{H}_{16}$ ). Moreover, a Scanning Mobility Particle Sizer (SMPS; TSI Inc.) was used to estimate the optical contribution of particles smaller than GRASP's smallest size bins.

The PI-Neph, PSAP, and integrating nephelometer all sampled from the LARGE inlet, which has a 50% passing efficiency at an aerodynamic radius of  $1.8 \mu\text{m}$  (McNaughton et al., 2007). The residence time within the PI-Neph was on the order of 30 and 15 s of acquisition time was required for each measured wavelength (three-wavelength SEAC<sup>4</sup>RS measurements took 45 s total). The integrated scattering and absorption measurements were both made at one hertz. In SEAC<sup>4</sup>RS, the PSAP data were bulk averaged with 15-s intervals for altitudes under 1,070 m and with 60-s intervals above 1,070 m. The corresponding details for the ancillary instrumentation can be found in Espinosa et al. (2018), which describes the calcification scheme in greater detail.

## 2.2. Data Standardization and Coregistration

The GRASP retrieval is significantly simplified if a given set of observations can be coregistered to a single point in space and time, ideally without an excessive number of unique wavelengths among the measurement inputs. In order to reduce the number of individual inversions performed, time averages of the raw PI-Neph and PSAP measurements were obtained over periods corresponding to high and stable aerosol loading. These averages, hereinafter referred to as a "samples," are composed of a phase function vector, degree of linear polarization vector, and single absorption coefficient scalar at each measured wavelength, derived from consecutive data obtain over periods ranging from 45 s to several minutes. An individual sample can then either constitute the entire input into a given GRASP retrieval or these samples can be averaged to obtain aerosol type specific "sample averages" that can also serve as inversion inputs.

A significant fraction of PI-Neph measurements occurred at very low aerosol concentrations, typically during high altitude transit legs of the flights. This fact, along with the large volume of PI-Neph data overall, motivated the decision to subselect and average the raw PI-Neph measurements into samples that were

composed of stable, high-quality data. Measurement periods where the total scattering was less than  $10 \text{ Mm}^{-1}$  or the change in integrated scattering between two adjacent raw measurements was greater than 15 % were first discarded. The remaining measurements were averaged over periods composed of at least three raw PI-Neph measurements whose individual angularly integrated scattering values summed to greater than  $200 \text{ Mm}^{-1}$ . This threshold was chosen to ensure that temporally uncorrelated sources of noise (e.g., photon counting noise, insufficient number of scatters in the sample volume, and CCD thermal noise) were significantly less than the measured  $F_{11}$  value. This procedure resulted in 573 SEAC<sup>4</sup>RS averages and 1,817 DC3 averages, with mean averaging times of 152 and 67.6 s, respectively.

The value of  $\beta_{abs}$  in each sample was obtained by taking the mean of all PSAP measurements obtained during the PI-Neph averaging window described in the previous paragraph. In 172 and 3 of the classified DC3 and SEAC<sup>4</sup>RS samples, respectively, no PSAP measurements were available within the averaging window. In these cases, only PI-Neph data were input into the GRASP retrieval, and  $\beta_{abs}$  was left unconstrained at all wavelengths. A small correction based on power law fits (i.e., absorption Angstrom exponent) was used to bring the 470-nm PSAP data to the PI-Neph's 473-nm channel. As corrected 660-nm PSAP data were not available during SEAC<sup>4</sup>RS and PI-Neph measurements were only made at 532 nm during DC3, no attempt was made in either campaign to obtain a value of  $\beta_{abs}$  that corresponded to the 671-nm scattering matrix measurements.

### 2.3. Classification of Samples by Aerosol Type

An aerosol classification scheme (Espinosa et al., 2018) is then used to estimate the dominate source of each aerosol by focusing on additional properties of the air mass associated with each measurement. The SEAC<sup>4</sup>RS data were subdivided into four categories corresponding to dust, biogenic, urban, and BB emissions. The PALMS instrument and aerodynamic size distributions were used to identify aerosols dominated by desert dust. Trace gas concentrations are then used to distinguish the remaining three SEAC<sup>4</sup>RS aerosol types, with  $\text{NO}_2$  used to identify urban and industrial emissions, carbon monoxide, and acetonitrile serving as correlates for BB plumes and isoprene and monoterpenes serving to identify heavy biogenic influence. It should be noted that the data classified as biogenic simply had significantly higher than background concentrations of gasses that are primarily associated with biogenic activity. These particle populations are therefore not necessarily exclusively of biogenic origin and, in many cases, likely represent the confluence of biogenic and anthropogenic emissions.

The scheme developed to categorize the DC3 samples was based on the aircraft's proximity to three storm domains outlined in the DC3 science objectives (Barth et al., 2015). These three domains were located over northern Colorado (CO), northern Alabama (AL), or the northern Texas and Oklahoma region (TX/OK). As convective systems have the potential to significantly influence aerosol properties (Corr et al., 2016; Eck et al., 2014; Jeong & Li, 2010), different classification schemes were applied to the DC3 data set (near convective systems) and the SEAC<sup>4</sup>RS data set (generally far from convective systems). Aerosol optical properties were intentionally omitted from all classification metrics to ensure independence between the classification scheme and the scattering features measured by the PI-Neph and PSAP.

Both the DC3 and SEAC<sup>4</sup>RS classification schemes employed here only allow one aerosol type to be assigned to a given sample. If a sample's ancillary data do not meet any of the classification conditions, the sample is assigned to an "unclassified" category. Furthermore, a sample is identified as "unclassified" if no single type is assigned to the majority of individual measurements composing that sample. Table 1 shows the number of samples this ancillary data classification scheme assigned to each category, as well as the number of unique flights containing at least one of the corresponding samples. All categories have cases originating from multiple flight days, increasing the likelihood that a given category average is representative of the corresponding type as a whole. Additionally, the type averaged integrated scattering coefficient  $\bar{\beta}_{sca}$  and asymmetry parameter  $\bar{g}$  at 532 nm is shown for reference. The final column of Table 1, representing the number of cases for which the mean residual between GRASP's fit and the  $F_{11}$  measurements was less than 10%, will be discussed further in section 4.1.

In the summer months, biogenic and urban emissions often dominate the SEUS while the western portion of the country is frequently influenced by wildfire smoke (Goldstein et al., 2009; Malm et al., 2004). While the SEAC<sup>4</sup>RS categories are not determined by location, clear spatial patterns emerge that are in strong agreement with these physical expectations. The urban classification is generally selected around city

**Table 1**  
Summary of Key Sampling Statistics by Aerosol Type

Aerosol type	No. of cases	No. of flights	$\beta_{sca}$ ( $Mm^{-1}$ )	g	RES < 10%
BB	105	8	$154 \pm 127$	$0.61 \pm 0.02$	99.0 %
Biogenic	252	14	$76.3 \pm 31.6$	$0.63 \pm 0.03$	93.6 %
Urban	28	10	$93.4 \pm 45.1$	$0.62 \pm 0.06$	92.9 %
Dust	15	2	$69.7 \pm 23.3$	$0.77 \pm 0.05$	0.00 %
CO Storms	329	5	$31.2 \pm 13.5$	$0.59 \pm 0.04$	73.6 %
TX/OK Storms	535	5	$52.4 \pm 14.9$	$0.59 \pm 0.03$	97.9 %
AL Storms	140	2	$57.0 \pm 21.7$	$0.62 \pm 0.02$	99.2 %
Unclassified	986	35	$55.0 \pm 43.0$	$0.58 \pm 0.09$	68.7 %
All Cases	2390	37	$58.4 \pm 39.7$	$0.59 \pm 0.05$	81.5 %

*Note.* Shown are the total number of cases, the number of unique flights for which at least one case was present as well as the mean and standard deviation of the measured 532-nm scattering coefficient ( $\beta_{sca}$ ) and asymmetry parameter (g) values. The final column indicates the percentage of cases for which the residual between the GRASP fit and the measured  $F_{11}(\theta)$  values at 532 nm was less than 10%.

centers like Houston and Dallas Texas as well as near the Ohio River Valley, a region known to have high levels of industrial activity. Additionally, the 15 points that met the requirements of the dust classification all correspond to a transported Saharan Air Layer that was present over Louisiana and the northern Gulf of Mexico at the start of the campaign (Ziembra et al., 2016). Back-trajectory calculations (Peterson et al., 2015; Toon et al., 2016) indicate that the majority of samples that were classified as BB originated predominantly from the California Rim Fire (58%), with the overwhelming majority of the remaining cases coming from smaller wildfires within the United States, primarily from three fires located in Wyoming, Colorado, and Kansas. The majority of these smoke plumes were relatively aged, with the freshest samples obtained just over 100 km downwind of the Rim Fire on 26 August. Forward trajectories from the National Oceanic and Atmospheric Administration Air Resources Laboratory Hybrid Single-Particle Lagrangian Integrated Trajectory model (HYSPPLIT; Stein et al., 2015) indicate that these samples were between 5 and 8 hr old, depending on injection height. The exact geographic locations of all classified samples, according to their assigned type, can be found in Espinosa et al. (2018).

In addition to the geographic consistency of the ancillary data classification scheme, very strong relationships were found between the angular scattering measurements and the aerosol type. A method was devised for predicting the ancillary classification results using only the PI-Neph light scattering measurements (Espinosa et al., 2018), and all but one aerosol type was predicted correctly more than 80% of the time. The agreement between the ancillary data and scattering-based classifications was much lower in the case of the AL storm category (recall of 47%). Many of these samples were found to have optical properties very similar to the biogenic samples, which is not surprising given that the AL storm domain corresponds to a region that was dominated by biogenic emissions during SEAC<sup>4</sup>RS.

### 3. Retrieval Methodology

Classification in itself is only the first step in characterizing aerosol optical properties or deriving an aerosol model. Here we obtain these optical properties by applying the GRASP inversion algorithm to measurements made by the PI-Neph and PSAP, resulting in retrieved values for PSD, complex refractive index, and fraction of spherical particles (SPH). GRASP is a versatile software package capable of retrieving a wide range of properties from a variety of data sets, while making fewer assumptions about the aerosol than traditional in situ or remote sensing retrieval algorithms (Dubovik et al., 2011, 2014). The inversion is performed making use of multiterm least squares fitting (Dubovik, 2004), allowing for different types of observations and multiple a priori constraints to be easily combined into a single inversion. The application of GRASP to PI-Neph data alone has been shown to produce retrievals of size distribution that are at least as accurate as those produced with common dedicated particle sizing instrumentation and retrievals of real refractive indices of particles on known chemical composition that closely match existing measurements (Espinosa et al., 2017). The incorporation of the PSAP absorption coefficient measurement is expected to bring the

accuracy of retrieved imaginary refractive index inline with these other parameters. A detailed analysis of the errors associated with these retrieved parameters is provided in section 3.3.

The retrievals were performed by inverting the  $F_{11}$ ,  $-F_{12}/F_{11}$ , and  $\beta_{abs}$  measurements simultaneously for each sample. As a result of instrument noise the measured values of  $F_{11}(\theta)$  and  $\beta_{abs}$  were occasionally less than zero, and the absolute magnitude of  $F_{12}(\theta)$  is sometimes greater than  $F_{11}(\theta)$ . If present, these nonphysical measurement values were excluded, and the retrieval is performed using only the remaining data. In each sample, the overwhelming majority of data points corresponded to physically possible values so entire samples were never discarded due to an excessive number of nonphysical values. The inversions of the SEAC<sup>4</sup>RS data incorporate all three PI-Neph wavelengths, but retrievals of DC3 data were limited to 532-nm data, as the red and blue channels were not available at the time of this campaign. The retrieval is applied both to the 2,390 individual samples and sample averages corresponding to the average measurements of six different aerosol types. In all samples of the seventh, dust-type GRASP failed to adequately reproduce the measured angular scattering patterns with sufficient fidelity to justify including these samples in the bulk of the analysis presented here. A detailed discussion of the GRASP fits is presented in section 4.1, but it is important to emphasize that measurement error, not retrieval assumptions, likely drove the poor fitting of these dust samples.

### 3.1. Aerosol Representation

#### 3.1.1. Assumptions Configured in the GRASP Retrieval

The flexibility built into the design of GRASP allows the user to select the assumptions that best match the information content of a particular data set. In this work, GRASP size distributions were modeled with 16 logarithmically spaced size bins, spanning 0.065 to 3.9  $\mu\text{m}$  in radius. It will be shown that, given realistic PSDs, the particles at the lower end of this size range generally contribute very little signal to ensemble type, light scattering measurement. The upper bound was chosen to include the vast majority of coarse mode particles capable of passing through the LARGE inlet. In all retrievals, the shape of the size distribution is only constrained by a smoothness parameter, and no assumptions about the number of modes are made. Additionally, two size bins centered around  $r = 0.05\mu\text{m}$  and  $r = 5\mu\text{m}$  were included but forced to zero in order to encourage the tails of the retrieved size distribution to trend toward zero.

While the aerosols measured in this work can still have significant number concentrations below 0.065  $\mu\text{m}$ , these particles generally possess very low scattering efficiencies and have a negligible contribution to the total amount of visible light scattered by a typical atmospheric aerosol. To better quantify the effect of these particles, the SMPS size distribution, which extends down to  $r = 0.005\mu\text{m}$ , was stitched to the size distribution retrieved by GRASP, and the resulting PSDs were averaged over the entire SEAC<sup>4</sup>RS experiment. A Mie code (Mishchenko et al., 2002) was then used to estimate the total amount of 532 nm light scattered by particles smaller than the center diameter of the first nonzero size bin ( $r = 0.065\mu\text{m}$ ). It was found that these particles were responsible for only 0.1% of the total light scattered by the stitched size distribution. As the shape of  $F_{11}$  can depend significantly on size parameter the contribution of these particles to the absolute phase function was also examined. It was found that the particles with radii smaller than 0.065  $\mu\text{m}$  had the largest contribution to  $F_{11}$  at scattering angles around 152°, where they made up only 0.9% of the total signal. Additionally, the tiny scattering signal produced by the smallest particles can be, to some extent, transferred into other size bins (and potentially very small changes in refractive index) producing an “optically equivalent” set of parameters. Therefore, we do not expect the ability of the retrieved parameters to reproduce the true optical properties of the aerosol in question to be significantly hindered by GRASP’s exclusion of the smallest particle sizes.

The search space for the real part of the refractive index is semicontinuous between 1.33 and 1.7, while the imaginary part can range from 0 to  $10^{-1}$ . The refractive index is held constant with respect to size, but, in the case of the multiwavelength SEAC<sup>4</sup>RS data, it is allowed to vary as a function of wavelength. This constraint is equivalent to the assumption that each sample can be modeled as if all particles possessed the same composition. The use of a single spectral dependent “effective refractive index” has been shown to reproduce the optical properties of both internally and externally mixed particles with high fidelity under many realistic circumstances (Dubovik et al., 2000; Mishchenko et al., 2016).

GRASP’s aerosol model assumes a mixture of spheres and spheroids. The spheroid component utilizes a fixed axis ratio distribution that was derived by Dubovik et al. (2006) from feldspar measurements made by Volten et al. (2001). The applications of this approach in AERONET operational inversions and satellite

remote sensing applications did not reveal any evident deficiencies (Dubovik et al., 2011). Furthermore, the results of section 4.1 suggest that this combination of spheres and spheroids is capable of reproducing the measured optical properties in this work with high fidelity.

GRASP provides a statistically optimized inversion in the presence of measurement errors. Therefore, the measurement uncertainties provided to GRASP are an important component of the retrieval and influence the algorithm's accuracy. The instrument characteristics dominating the expected error can be attributed primarily to calibration and laser power uncertainties, which produce effects that are frequently independent of scattering angle. Correspondingly, simulations of PI-Neph error suggest that the relative uncertainty in the  $F_{11}$  measurement is approximately constant with angle. Similarly, the simulated absolute error in  $-F_{12}/F_{11}$  was also found to be relatively constant at all angles. A single uncertainty value for each measurement type at each wavelength was therefore used in the inversion. These error values were initially calculated from the results of the error simulations described in section 3.3.1. By running representative test cases through a Monte Carlo simulation (section 3.3), it was found that small adjustments to these initial calculated uncertainty estimates produced more accurate retrievals. These slight differences between calculated and empirically determined uncertainties likely stem from complexities like correlations in the errors between angles, which are not included in our current configuration of GRASP. The final  $1\sigma$  uncertainties provided to GRASP associated with the 532-nm data were 6% and 0.06 in  $F_{11}$  and  $-F_{12}/F_{11}$ , respectively. In the red and blue channels, which had more random variation in the power of the laser source, a value of 20% and 0.09 were estimated as  $F_{11}$  and  $-F_{12}/F_{11}$  uncertainties, respectively. The absorption coefficient uncertainty was estimated at  $0.63 \text{ Mm}^{-1}$  for all wavelengths.

### 3.1.2. Parameterization of the Retrieved Size Distributions

To construct an easily accessible aerosol model, we obtain lognormal-based parameterizations of the 16 bin size distributions retrieved by GRASP. In these parameterizations, the fine and coarse particles are treated separately, with the separation between the two particles populations being defined by the minimum in the retrieved size distribution closest to  $r = 0.5 \mu\text{m}$ . In the overwhelming majority of 16 bin size distributions retrieved by GRASP, a clear minimum was observed in this region. The metrics used to characterize each mode of the PSD are chosen to be consistent with the parameterizations used in Dubovik et al. (2002). Specifically, the volume median radius  $r_v$ , standard deviation of the volume median radius  $\sigma$ , and volume concentrations  $C_v$  are all provided along with the one standard error estimates in the corresponding retrieved values. While the retrieved modes of the size distributions do not exactly match lognormal distributions, these parameters were chosen to match those of true lognormal size distributions if a real lognormal mode was observed (Dubovik et al., 2002).

## 3.2. PSAP as a Constraint on Aerosol Absorption

Variations in the imaginary refractive index can produce small changes in the angular dependence of the scattered light that can potentially provide information regarding an aerosol's tendency to absorb light. However, under typical measurement conditions instrument uncertainty often exceeds the changes resulting from typical variability in  $k$ , limiting sensitivity to this parameter when only light scattering data are inverted. In this work, we add PSAP absorption measurements to the more established PI-Neph inversion in an effort to better constrain the retrieved imaginary refractive index. As far as the authors are aware, this represents the first time a filter-based absorption measurement has been combined with polar nephelometer data to obtain a comprehensive set of aerosol properties. The combination of these two data sets provides sensitivity to all important optical properties of an aerosol and the retrieved parameters should, in principle, be highly consistent with the true radiative properties of the particles. However, significant corrections are required when obtaining absorption coefficient from changes in filter transmission and the corresponding values of  $\beta_{\text{abs}}$  can contain large uncertainties themselves (Bond et al., 1999; Virkkula, 2010). In this section we evaluate the changes in the SEAC<sup>4</sup>RS and DC3 retrievals produced by the inclusion of the PSAP measurements of  $\beta_{\text{abs}}$  as an additional input into the inversion.

### 3.2.1. Sensitivity to Absorption in the Angular Scattering Data Alone

We can look explicitly at the sensitivity to absorption contained within the PI-Neph measurement by examining the changes in  $F_{11}$  and  $-F_{12}/F_{11}$  that occur over a realistic set of  $k$  values. Figure 1 shows phase function and degree of linear polarization for combinations of spherical and spheroidal particles representative of the fine mode aerosol ( $r < 0.5 \mu\text{m}$ ) observed during SEAC<sup>4</sup>RS and DC3. The black  $F_{11}$  and  $-F_{12}/F_{11}$  curves are the same among all four plots and represent the mean GRASP fit at 532 nm of the fine mode particles sampled during these two campaigns. The blue and red curves represent the theoretical fits given the 5th and



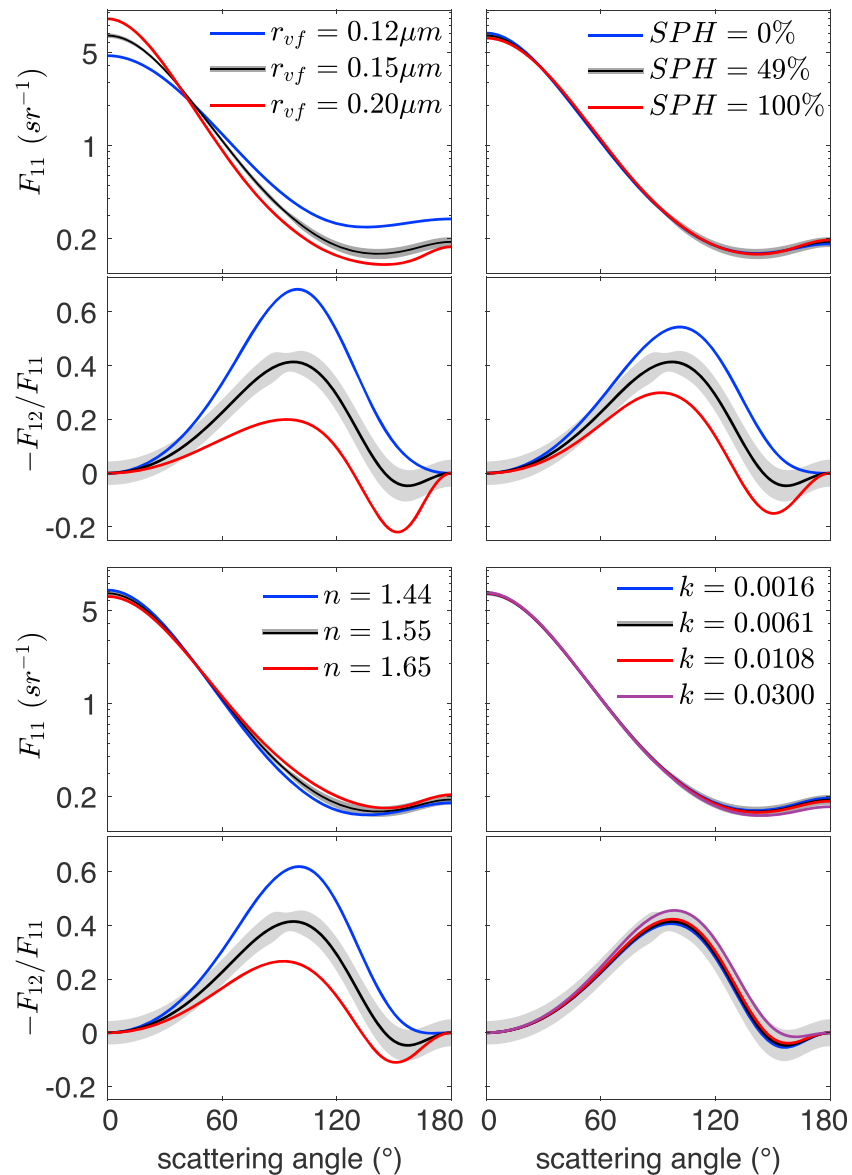


**Figure 1.** The mean values (black) of the 532 nm  $F_{11}$  and  $-F_{12}/F_{11}$  GRASP fits for the fine mode of the SEAC<sup>4</sup>RS measurements. The theoretical values given the 5th (blue) and 95th (red) percentiles of the retrieved volume median fine mode radius ( $r_{vf}$ ), spherical fraction ( $SPH$ ), real refractive index ( $n$ ), and imaginary refractive index ( $k$ ) are shown in comparison. The gray region denotes the  $1\sigma$  uncertainty window of the Polarized Imaging Nephelometer measurement.

95th percentiles, respectively, of the corresponding retrieved values with all other parameters held constant. For example, the blue line of the upper left subplot shows the theoretical  $F_{11}$  value given the mean fine mode size distribution shape, complex refractive index, and spherical fraction but with the volume median radius shifted to the lower 5th percentile of the retrieved values ( $r_{vf} = 0.114\mu\text{m}$ ). In the plots showing changes produced by different imaginary refractive indices (bottom right), an extra purple curve is added at  $k = 0.03$  in order to make the changes in scattering patterns more visible. The spread of the lines in these plots provides a sense of the sensitivity of  $F_{11}$  and  $-F_{12}/F_{11}$  to changes in the corresponding parameter, given a fine mode-dominated aerosol. In the SEAC<sup>4</sup>RS inversions, additional sensitivity to a given parameter may also often be found in the spectral dependence of the retrieval inputs, which has been omitted here for brevity.

The most apparent feature of Figure 1 is that there are only small changes in the theoretical  $F_{11}$  and  $-F_{12}/F_{11}$  values over the bulk of the range of imaginary refractive index values observed during these two campaigns.

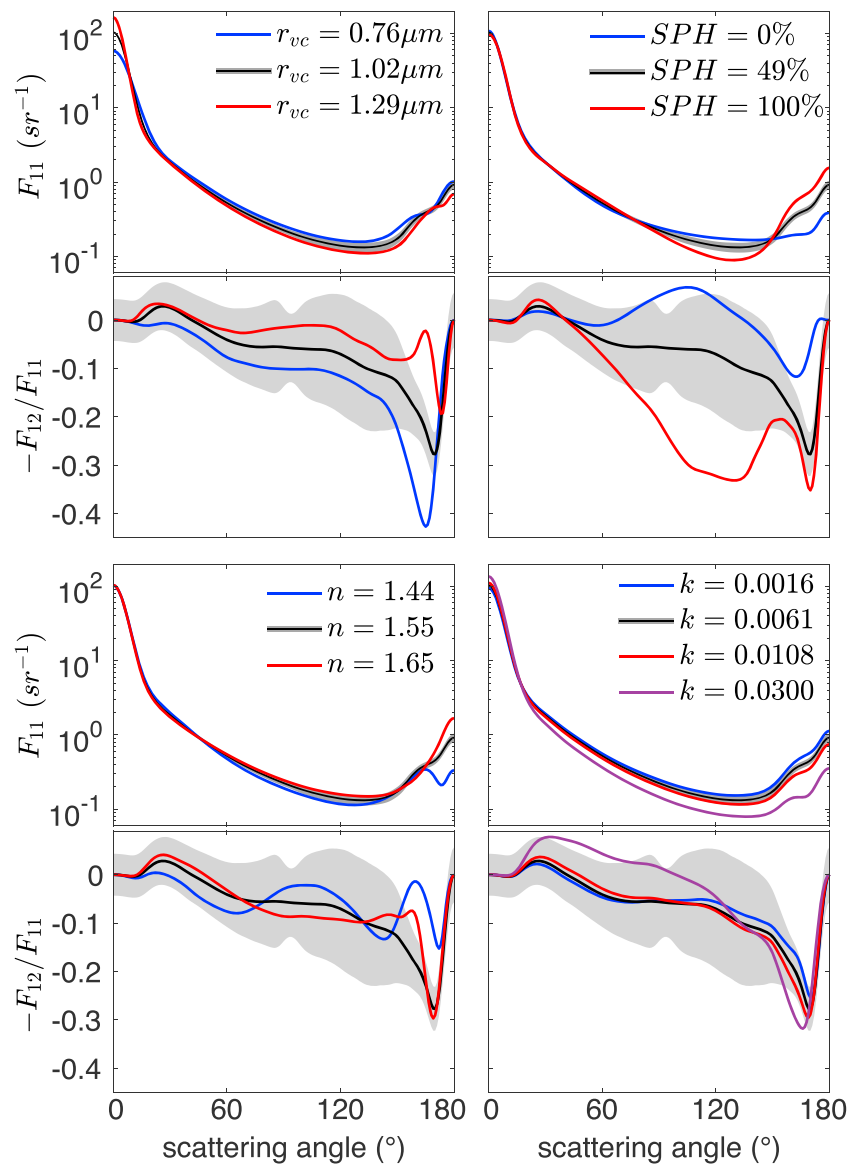


**Figure 2.** The mean values (black) of the 532 nm  $F_{11}$  and  $-F_{12}/F_{11}$  GRASP fits for the coarse mode of the SEAC<sup>4</sup>RS measurements. The theoretical values given the 5th (blue) and 95th (red) percentiles of the retrieved volume median coarse mode radius ( $r_{vc}$ ), spherical fraction (SPH), real refractive index ( $n$ ), and imaginary refractive index ( $k$ ) are shown in comparison. The gray region denotes the  $1\sigma$  uncertainty window of the Polarized Imaging Nephelometer measurement.

At all angles, these changes are smaller than the uncertainty of the PI-Neph measurement (gray shading), so very little sensitivity to  $k$  is expected without the aid of additional information. Furthermore, the changes in  $-F_{12}/F_{11}$  produced by different  $k$  values mimic changes that are observed in  $r_{vc}$ ,  $n$ , and spherical fraction, complicating attribution of these features. This implies that, given a fine mode-dominated aerosol, changes in these variables are almost indistinguishable from changes in  $k$  within the scope of PI-Neph data.

It will be shown in section 4.2.2 that the bulk of the aerosols sampled in DC3 and SEAC<sup>4</sup>RS are fine mode dominated, so the retrievals in this work are best contextualized by the fine mode curves of Figure 1. However, it is also important to examine theoretical  $F_{11}$  and  $-F_{12}/F_{11}$  values corresponding to the coarse mode particles, as these angular scattering patterns can differ markedly from their fine mode counterparts and some of the aerosol types explored (e.g., CO storms) can have a significant component of coarse particles. Figure 2 shows the coarse mode component of the  $F_{11}$  and  $-F_{12}/F_{11}$  curves corresponding to the mean,

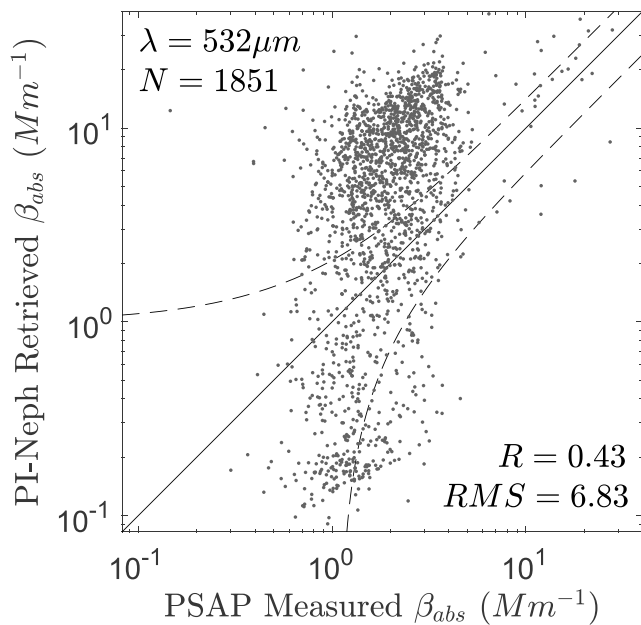


**Figure 3.** A comparison of the 532-nm Particle Soot Absorption Photometer (PSAP) absorption coefficient measurements with the GRASP retrievals of absorption using only Polarized Imaging Nephelometer (PI-Neph) data. A weak correlation is observed between the two data sets, but the majority of the PI-Neph only retrievals fall outside the assumed 95% uncertainty window of the PSAP (dashed lines).

5th and 95th percentiles of the retrieved values. Significantly more variation exists among the coarse mode scattering patterns of the various  $k$  values than in the fine mode case.

In order to assess the impacts of including PSAP data, the GRASP retrieval was first run on the SEAC<sup>4</sup>RS and DC3  $F_{11}$  and  $-F_{12}/F_{11}$  measurements alone, without the inclusion of the absorption measurements. A scatter plot comparing the absorption coefficients retrieved using this PI-Neph only inversion and the corresponding values of  $\beta_{abs}$  measured independently by the PSAP at 532 nm is shown in Figure 3. The dashed lines represent the estimated  $2\sigma$  uncertainty window of the PSAP measurement based on the 20% relative error scenario described in section 3.3, which represents our best estimate of the instrument's uncertainty. Overall, a correlation coefficient of 0.43 was obtained between the two data sets, suggesting some limited sensitivity to  $\beta_{abs}$  in the PI-Neph-only retrievals. However, it is clear that the retrieved values are considerably higher on average than the measured quantities, with the bulk of the retrievals falling above the PSAP's 95% uncertainty window. Furthermore, the retrieved values contain an order of magnitude more variability than the measurements. While the PSAP measurement may contain systematic biases and random noise, there is no obvious reason to expect the variability in the measured values to underestimate the true variability of the sampled aerosol. This suggests that the higher variability in the retrieved absorption results primarily from retrieval uncertainties stemming from insufficient sensitivity to absorption in the light scattering measurements.

### 3.2.2. Influence of PSAP Absorption Data in the Joint Retrieval

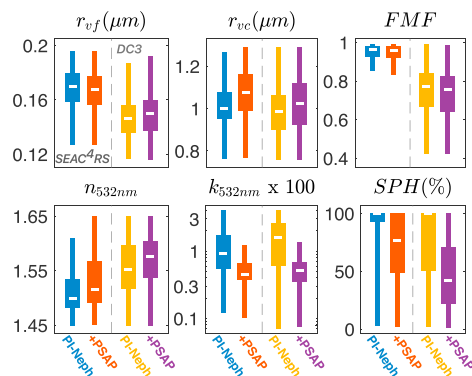
A joint retrieval was then run on the PI-Neph and PSAP data simultaneously, and the results were compared against the PI-Neph only inversion.

Figure 4 shows the changes in the campaign specific distribution of key retrieved parameters with and without the inclusion of PSAP data. A very large reduction in the variability of  $k$  can be seen after the inclusion of PSAP, suggesting that the absorption measurement is providing a useful constraint on the retrieval. The reason for the corresponding drop in the median imaginary refractive index is not obvious but likely results in part from a combination of the reduced erroneous variability and the limitation that  $k > 0$ .

The corresponding drop in the median imaginary refractive index likely results primarily from the combination of this reduced erroneous variability, and the fact that GRASP requires  $k > 0$ .

A significant increase in median real refractive index and decrease in median spherical fraction are also seen after the PSAP data are included. It can be seen from Figure 1 that as the values of  $k$  decreases the peak maxima of the  $-F_{12}/F_{11}$  fit will be reduced along with a small increase in  $F_{11}$  at scattering angles close to  $180^\circ$ . In most of the retrievals GRASP offsets these changes in the fit through a combination of a reduced spherical fraction and a slight increase in  $n$ , both of which have similar scattering angle dependencies as  $k$ . GRASP's ability to "trade" attribution of different scattering features between different variables emphasizes the fundamental limitations of the retrieval produced by the nonuniqueness of the solution space. From this perspective, it is clear that constraining absorption with the addition of the PSAP data has the potential to improve the accuracy of inverted parameters other than  $k$ . Another potential way to address this nonuniqueness would be to increase the number of measurement wavelengths within the PI-Neph, which can help to constrain spectrally independent parameters like size and spherical fraction.

Figure 2 suggests that the variety of scattering patterns produced by coarse mode particles is much higher than for the corresponding fine mode particles. These unique features may help to attribute scattering changes more directly to the underlying variables in the case of coarse mode dominated particle populations. For example, in the fine mode-dominated cases of DC3 and SEAC<sup>4</sup>RS it was observed that the addition of PSAP data can produce significant changes in spherical fraction and real refractive index, as these variables have scattering signatures that are similar to the signatures of  $k$ . The large differences in  $-F_{12}/F_{11}$



**Figure 4.** The change in the distribution of various retrieved parameters produced by the inclusion of Particle Soot Absorption Photometer’s (PSAP) absorption coefficient measurement. The retrieved parameters shown include the volume median radii of the fine ( $r_{vf}$ ) and coarse ( $r_{vc}$ ) modes, fine mode fraction (FMF), real ( $n_{532nm}$ ) and imaginary ( $k_{532nm}$ ) refractive indices at 532 nm, and spherical fraction (SPH). The blue and red bars represent the SEAC<sup>4</sup>RS retrievals with (“+PSAP”) and without (“PI-Neph”) the inclusion of the PSAP measurement, respectively. The yellow and purple bars represent the DC3 retrievals with and without the inclusion of the PSAP measurement, respectively. The white central mark indicates the median while the boxes denote the 25th and 75th percentiles with the whiskers extending to the 5th and 95th percentiles of the data.

at scattering angles between 90° and 120° resulting from different spherical fractions observed in coarse mode aerosols could potentially help separate changes in SPH from changes in complex refractive index. This fact, combined with a stronger direct dependence on  $k$  in the coarse mode scattering patterns, suggests that absorption may be able to be retrieved more accurately from light scattering data alone in a coarse mode dominate aerosol. It is important to note though that inlet cutoff effects produce a narrower, truncated coarse mode size distribution that is more prone to scattering features that occur with high angular frequency. Many of the unique features observed in Figure 2 may be washed out in simulations performed with more realistic particle populations, with a broader coarse mode.

### 3.3. Monte Carlo Based Error Estimation

In this section a Monte Carlo simulation designed to evaluate the benefits of incorporating PSAP data into the retrieval and, more generally, to estimate the uncertainties in the retrieved parameters is described. The synthetic data set used in the simulation is constructed by adding artificial noise to the  $F_{11}$ ,  $-F_{12}/F_{11}$ , and  $\beta_{abs}$  fits produced by the PI-Neph and PSAP combined retrievals of the DC3 and SEAC<sup>4</sup>RS measurements. By using the fits of the measurements to produce the synthetic data set, the retrieval uncertainties are estimated around points in the parameter space that correspond to the actual data. This synthetic data are then fed back into the GRASP inversion, and the retrieved parameters are compared

with the values used to generate the original fits. The process is then repeated 100 and 300 times for the DC3 and SEAC<sup>4</sup>RS fits, respectively, with different, randomly determined noise values used in each iteration. Fewer iterations are used in the DC3 simulations to keep the total number of iterations performed over both campaigns roughly equivalent (DC3 has approximately three times as many samples as SEAC<sup>4</sup>RS). A diagram of this process is shown in Figure 5.

#### 3.3.1. Simulated Measurement Errors

The noises used to generate these synthetic data sets should mimic the true instrument uncertainties as closely as possible. The PSAP uncertainty depends strongly on the validity of the particle assumptions composing the measurement adjustments (e.g., scattering correction) and is therefore difficult to estimate. Based on the findings of Virkkula et al. (2005) we have added a normally distributed absolute noise offset with a mean of zero and standard deviation of  $0.5 \text{ Mm}^{-1}$ . Additionally, we have added a relative noise component to the synthetic PSAP data that scales with the magnitude of the true value of  $\beta_{abs}$  in the simulation. A range of ground-based comparisons between PSAP and other instrumentation designed to measure absorption as well as theoretical expectations has produced one standard deviation relative uncertainty estimates ranging from a 3% to 15% (Bond et al., 2013; Müller et al., 2011; Schmid et al., 2006; Virkkula et al., 2005). In order to account for additional uncertainties associated with airborne sampling (e.g., varying RH and temperature and increased variability in aerosol flow rate), a one standard deviation relative uncertainty of 20% has been applied to the simulated PSAP data. A recent study by Mason et al. (2018) estimated the total PSAP uncertainty during SEAC<sup>4</sup>RS to be in this range, based on theoretical consideration as well as an intercomparison with other in situ absorption measurements made during the campaign. Moreover, an additional run of the simulation was performed using a PSAP relative uncertainty of 40%, primarily to confirm that the retrieved parameters other than  $k$  would not be negatively impacted if PSAP errors were significantly underestimated.

A comprehensive noise model was applied to the simulated PI-Neph data that took into account a wide range of error sources, including photon counting noise, instrument stray light, uncertainties in laser and detector geometries, light source power, and polarization drift as well as uncertainties in the scattering properties of the gasses used to calibrate the instrument. The primary advantage of this approach, over the simpler normally distributed relative and absolute noises applied to the PSAP data, is its ability to capture correlations in error that occurs between different scattering angles. All sources of uncertainty in the PI-Neph measurement, besides photon counting noise, produce some level of angular correlation in the resulting errors and the effects of these errors have on GRASP’s fitting of the data depend on their correlation lengths.

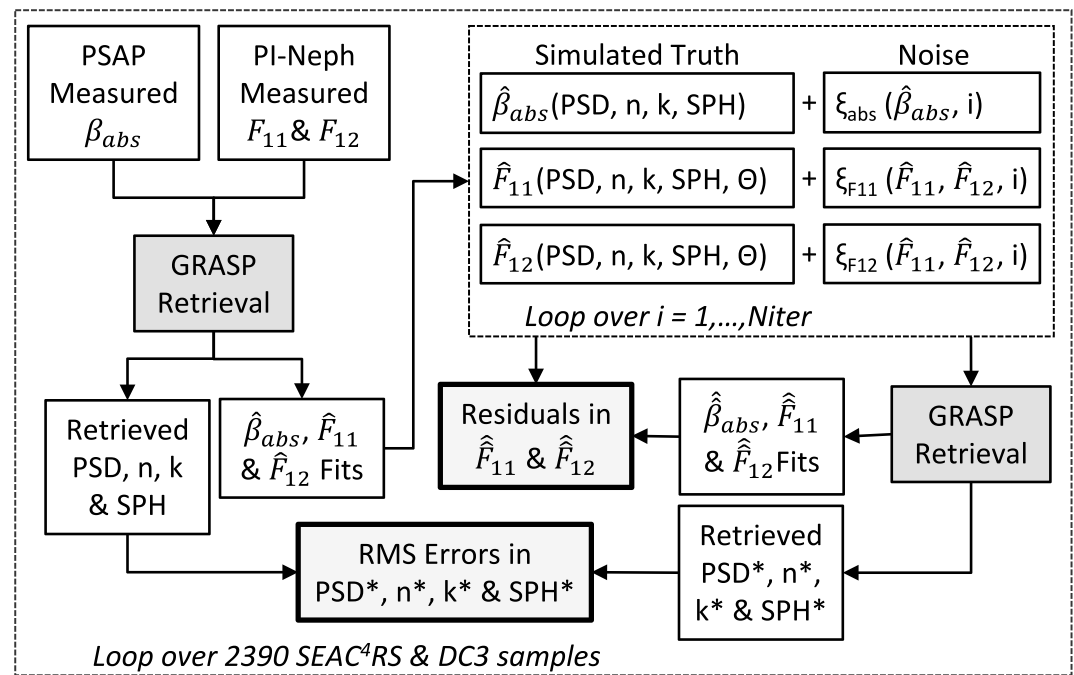


**Figure 5.** The Monte Carlo procedure used to estimate the retrieval errors. A synthetic data set is derived by adding instrument representative noise to the fits of the measured samples (denoted with single hats). Generalized Retrieval of Aerosol and Surface Properties (GRASP) is then used to fit these simulated measurements (fits of synthetic data are denoted with double hats) and the parameters retrieved from the synthetic data (denoted with an asterisk) are compared with the parameters retrieved from the true measurements that exactly reproduce the “simulated truth.” Niter was 300 for SEAC<sup>4</sup>RS samples but only 100 iterations were used in the DC3 simulations due to the higher computational demands associated with the larger number of samples obtained in this campaign. PSAP = Particle Soot Absorption Photometer; PI-Neph = Polarized Imaging Nephelometer; PSD = particle size distribution; SPH = spherical particles.

It is important to emphasize that, in the configuration used throughout this work, GRASP internally assumes uncorrelated, lognormally distributed errors for each individual measurement value. Since the PI-Neph errors simulated here are not necessarily consistent with these error assumptions, the uncertainty estimates derived may overestimate the uncertainties of an “ideal” retrieval in which the noise assumptions are perfectly matched to the instrument errors. Improved matching of GRASP’s error assumptions and the true PI-Neph error distributions, particularly in regards to correlations in error between neighboring scattering angles, is the subject of planned future work.

While a direct measure of PI-Neph error is not available for comparison against the simulated noise model, the GRASP residuals are expected to display strong sensitivity to measurement uncertainty. Table 2 compares the residuals obtained when fitting the real measurements with the residuals obtained in the Monte Carlo simulation utilizing the theoretical noise model. The residuals are found to be very similar for both the  $F_{11}$  and  $-F_{12}/F_{11}$  data sets among all three wavelengths and, in the case of DC3, across several different aerosol types. Additionally, when the true and Monte Carlo residuals deviate, the true residuals are typically lower than those making use of the theoretical noise model. This slight potential overestimation of PI-Neph error makes it unlikely that the resulting uncertainties obtained for the retrieved parameters are underestimated.

The PI-Neph residuals are strongly dependent on instrument error because the measurement is composed of several hundred strongly correlated values, whose combined errors cannot all be fit simultaneously. As the absorption coefficient is relatively independent from all other retrieval inputs, almost any value of  $\beta_{abs}$  can be fit, without significantly elevated retrieval residuals, if the appropriate value of  $k$  is chosen. This fact prohibits a meaningful residual-based assessment of the PSAP uncertainty estimate used here. It was found that the absorption residuals were consistently below 1% when fitting the true measurements as well as both the 20% and 40% relative error Monte Carlo scenarios. Furthermore, the small residuals that were observed

**Table 2**  
The Median Relative Residuals Between the Measurements and GRASP Fits of  $F_{11}$  and  $-F_{12}/F_{11}$  Over All Scattering Angles

Sample group	$F_{11}$		$-F_{12}/F_{11}$	
	TR	MC	TR	MC
SEAC <sup>4</sup> RS (473 nm)	0.075	0.076	0.093	0.100
SEAC <sup>4</sup> RS (532 nm)	0.045	0.044	0.056	0.060
SEAC <sup>4</sup> RS (671 nm)	0.095	0.100	0.091	0.104
DC3 CO (532 nm)	0.057	0.060	0.073	0.080
DC3 TX/OK (532 nm)	0.039	0.044	0.056	0.064
DC3 AL (532 nm)	0.033	0.044	0.049	0.064

*Note.* The true value (TR) derived from the field measurements is shown adjacent to the corresponding quantity from the Monte Carlo (MC) simulation. The strong agreement observed between the two values provides confidence in the simulated Polarized Imaging Nephelometer noise used in the MC trials.

in the absorption fits did not increase meaningfully between these two different relative error simulation conditions.

### 3.3.2. Resulting Uncertainties in the Individual Sample Retrievals

The Monte Carlo simulation was run with four different retrieval input scenarios using synthetic measurements composed of (1) only the  $F_{11}$  data set, (2) data from both the  $F_{11}$  and  $F_{12}$  scattering matrix elements, (3) scattering matrix and absorption coefficient data under the 20% relative error model, and (4) scattering matrix and absorption coefficient data under the 40% relative error model. Table 3 shows the typical errors of a variety of retrieved parameters, separated by campaign and input parameter scenario. The error values provided represent the root mean square errors (RMSEs) between the corresponding input value used to generate the fits, and the values retrieved after synthetic noise was added to the data. Separate RMSEs are first calculated for each of the 2,390 retrieval fits, and then the median is taken of all RMSEs from a given campaign. These medians can be interpreted as  $1\sigma$  uncertainty estimates for parameters retrieved from an individual sample.

The differences between the second and third scenarios are expected to most closely convey the effects of adding PSAP to the PI-Neph only retrieval. The

trends in the errors between these two scenarios generally support the conclusions of section 3.2. The most obvious benefit of including  $\beta_{abs}$  measurements into the retrieval is a reduction in the error of  $k$  by more than a factor of 4. Furthermore, we see slight reductions in the estimated uncertainties in the retrieved spherical fraction and real refractive index in some cases. While the improvement in  $k$  is slightly reduced, these conclusions generally hold true even in the event of the last scenario with 40% relative error in the absorption measurement. This implies that the inclusion of PSAP data is unlikely to negatively impact the retrieved spherical fractions or real refractive index, even if the error in the measurement is significantly underestimated by the 20% error scenario.

The retrieved parameters relating to size distribution responded less favorably to the inclusion of PSAP data, particularly in the simulations based on the DC3 samples. There were modest increases in the errors in the fine and coarse mode volume median radius as well as fine mode volume fraction (FMF) when PSAP data were included into the simulated retrievals of this campaign. Adding the absorption measurements to the SEAC<sup>4</sup>RS simulations produced fewer adverse effects on the retrieved PSD, with the addition of PSAP only producing a small increase in the RMSE of coarse mode volume median radius ( $r_{vc}$ ). As inlet cutoff effects already prevent the size distribution of the sampled coarse mode from accurately representing the ambient aerosol, these increased errors in the retrieval of coarse mode size distribution will not meaningfully degrade the value of the retrieval. Furthermore, the increased uncertainty in  $r_{vf}$  observed in the DC3 cases is small enough to justify the significant benefits in the accuracy of the retrieved imaginary refractive index.

Comparing the RMSE values between the scenarios with and without  $F_{12}$  data also provides an interesting exercise, as it allows us to quantify the benefits of including polarization in future measurements of angular light scattering. In general, these Monte Carlo simulations suggest that polarization does improve the quality of the inversions, especially in regards to the complex refractive index and fine mode volume median radius. However, the spherical fraction and  $r_{vc}$  RMSE values showed significant increases after the inclusion of the  $F_{12}$  data. A satisfactory explanation for these increases is not entirely apparent, but it is likely the result of inconsistencies between the PI-Neph error simulated in this numerical experiment and the error assumptions configured within GRASP.

In regards to the addition of polarization information, the results of this Monte Carlo-based sensitivity analysis is generally in agreement with the results of Li et al. (2009) and Fedarenka et al. (2016) obtained for polarimetric measurements made from ground-based (AERONET) radiometers. These studies demonstrated that the utilization of polarimetric measurements is useful for improving the retrieval of several parameters of fine mode aerosols. Specifically, improvements were observed in the real part of the refractive index and shape of the size distribution, two findings that are corroborated by the Monte Carlo simulations of this work. These authors also found that polarization slightly increased the accuracy of the retrieved fraction of spherical particles, although this finding is not mirrored in the present study. This discrepancy is most

**Table 3**

*The Median RMSE of the Retrieved Aerosol Properties for Individual Samples Given Different Inversion Input Scenarios*

Experiment	GRASP inputs	SPH (%)	$n_{532nm}$	$k_{532nm} \times 100$	$r_{vf}$ (nm)	$r_{ve}$ (nm)	FMF
DC3	$F_{11}$	46.8	0.12	2.82	14.8	103	0.097
	$F_{11}, F_{12}$	45.5	0.072	2.30	10.7	143	0.059
	$F_{11}, F_{12}, \beta_{abs}(20\%)$	37.1	0.069	0.44	11.7	165	0.069
	$F_{11}, F_{12}, \beta_{abs}(40\%)$	37.5	0.069	0.49	11.5	162	0.067
SEAC <sup>4</sup> RS	$F_{11}$	20.0	0.052	1.81	12.0	131	0.027
	$F_{11}, F_{12}$	35.9	0.044	1.34	9.94	163	0.029
	$F_{11}, F_{12}, \beta_{abs}(20\%)$	33.3	0.044	0.33	9.94	167	0.029
	$F_{11}, F_{12}, \beta_{abs}(40\%)$	33.0	0.044	0.55	9.92	169	0.030

Note. RMSE = root mean square error.  $\beta_{abs}(20\%)$  and  $\beta_{abs}(40\%)$  represent the simulated Particle Soot Absorption Photometer data with 20% and 40% relative errors, respectively.

likely due to differences in angular sampling, particle populations, and simulated instrument noise characteristics. However, it should be noted that the theoretical data shown in Figure 1 do suggest significant sensitivity to spherical fraction in the present measurements of  $-F_{12}/F_{11}$ , although the polarization changes observed closely mimic perturbations of several other fine mode parameters. In the coarse mode, Li et al. (2009) and Fedarenka et al. (2016) also did not find any significant improvements resulting from the addition of polarization. They attributed this to the fact that coarse mode particles, such as those of desert dust, are frequently nonspherical and tend to scatter only weakly polarized light (Dubovik et al., 2006). These two studies also found that the addition of polarization produced no significant effect on the retrieval of aerosol absorption. In the present work, we do find a slight decrease in the error of  $k$  when polarization is included, but the effect is relatively small.

#### 4. Results and Discussion

The above sensitivity analysis and quantification of expected error demonstrates that the joint inversion of PI-Neph and PSAP measurements can produce an accurate set of retrieved aerosol parameters representative of the optical properties of the particles at the measurement wavelengths. This permits an opportunity to provide useful characterizations of the size distribution, percent of spherical particles, and real and imaginary parts of the refractive index for the different aerosol types identified during DC3 and SEAC<sup>4</sup>RS. These unique results provide a comprehensive and optically consistent summary of aerosol properties for different aerosol types prevalent in the summer time contiguous United States.

Two retrieval approaches have been applied in the following section in order to obtain metrics of size distribution, percentage of spherical particles, and complex refractive index representative of each aerosol type. The first method involves applying the inversion to each of the 2,390 samples independently and then grouping the resulting retrieved values by aerosol type. The resulting individual sample retrievals present an opportunity to explore the variability of each parameter. The second method is to directly invert the sample averages, which are composed of the mean of all PI-Neph and PSAP samples associated with a given aerosol type. In the latter approach, the inversion is applied only once for each of the six types examined, which can reduce noise patterns that can potentially lead to consistent artifacts in the retrieved parameters. Additionally, the Monte Carlo methods of section 3.3 are more directly applicable to these retrievals of sample averages. In the end, however, it was found that the overall results of the retrieve-then-average and average-then-retrieve approaches did not differ significantly.

The goal of this section is to present fully characterized aerosol models based on the application of the GRASP inversion to the DC3 and SEAC<sup>4</sup>RS measurements, classified into six aerosol types. The first step, though, is to test the assumptions in the GRASP inversion by analyzing how well the retrieval can reproduce the input measurements. The retrieved parameters will then be presented both as statistics pertaining to all cases of a given aerosol category and as single values summarizing each type. Unless explicitly stated otherwise, all samples with phase function fit residuals greater than 10% are excluded from the analysis presented in this section. This threshold roughly corresponds to twice the median 532 nm absolute  $F_{11}$  residual.

#### 4.1. Measurements and Retrieval Fits

##### 4.1.1. Proportion of Cases With Acceptable $F_{11}$ Residuals

The final column of Table 1 shows the percentages of cases that had  $F_{11}$  GRASP residuals that met the 10% threshold condition. Unfortunately, none of the dust cases met this condition, and this class was therefore excluded from the following analysis. The total scattering was reasonably high for many of the dust samples, but the strong forward scattering peak produced by these aerosols means that the majority of the scattered energy is directed into the low scattering angles. In turn, the angular scattering intensities at higher scattering angles were often very weak and dominated by instrument noise. Additionally, the bulk of the scattered light in these dust samples was driven by relatively few large dust particles, resulting in very limited particle statistics within the PI-Neph's sampling volume. These errors likely had significant impact, both on the quality of the retrieval fit but also on the accuracy of the retrieved parameters, like real refractive index, which are highly sensitive to the backward scattering angles (Zhao et al., 1997). It is important to note that the features driving the large residuals in the dust samples were consistent with the expected PI-Neph errors and no evidence was found, suggesting that GRASP's aerosol assumptions were incapable of reproducing the scattering features of these large, likely nonspherical, particles.

In all other aerosol categories the percentage of cases meeting the 10% residual condition were quite high, often greater than 90%. Of the classified cases, the CO storm samples had the lowest percentage of satisfactory residuals, with just 74% of cases meeting the threshold. The poorer fit quality of these samples is at least partially driven by very low particle concentrations found during the corresponding measurement periods. Additionally, the CO storm observations contained a significant coarse mode, which, as in the case of the dust samples, drove a large fraction of the scattered light into the forward angles. The large number of unclassified points with residuals greater than 10% is primarily driven by very low aerosol loading, with the majority of these cases producing less than  $22 \text{ Mm}^{-1}$  of total scattering (the mean is skewed significantly higher by a small number of samples with very strong scattering). In the other categories many of the residuals are quite low, often less than what is expected between the true value and the PI-Neph measurement given instrumental errors alone. This suggests that GRASP is fitting some features of the measurement that correspond to instrumental artifacts.

##### 4.1.2. Scattering Matrix Measurements and Fits for Sample Averages

Figure 6 shows  $F_{11}$  and  $-F_{12}/F_{11}$  sample averages for the three DC3 storm domains as well as the biogenic and BB aerosols from SEAC<sup>4</sup>RS along with the corresponding GRASP fits. The GRASP fit generally reproduces the input measurements well, capturing the unique features of each aerosol type. A progression in both the  $F_{11}$  and  $-F_{12}/F_{11}$  sample averages is evident as the DC3 storm domains transition from AL to TX/OK to CO. The increase in forward scattering peak observed through this sequence suggests an increased scattering contribution from particles in the larger size ranges that direct the bulk of their scattered energy into the lowest scattering angles (Russell et al., 2004). The averaged  $F_{11}$  data, corresponding to the SEAC<sup>4</sup>RS BB and biogenic categories, show very weak forward scattering and thus suggests relatively few coarse mode particles. It is found in section 4.2.2 that the fine mode particles of the SEAC<sup>4</sup>RS samples tended to have slightly larger diameters than their DC3 counterparts. In the fine mode, the height of the  $-F_{12}/F_{11}$  maximum is strongly dependent on  $r_{\text{vf}}$  (see Figure 1), and it is likely that the reduced polarization observed in the SEAC<sup>4</sup>RS cases is attributable to these larger fine mode particles. Among the SEAC<sup>4</sup>RS fine mode-dominated samples, the  $-F_{12}/F_{11}$  peak was slightly higher on average in the BB cases, with this feature most clearly separating the BB aerosols from the other two types. Additionally, small differences in the shape of  $F_{11}$  can also be observed in the BB averages, with the relative contribution from the extreme forward and backward scattering angles being slightly suppressed relative to the other two types.

The variability within a given type's angular scattering patterns (not shown) was the highest in the case of the samples associated with urban emissions. Further examination of this variability showed two distinct subgroups, with the conditions around the Ohio River Valley differing significantly from conditions near urban centers (scattering matrix elements shown in Figure S1 in the supporting information). The starkest difference between these two subgroups occurred in the  $-F_{12}/F_{11}$  maxima, with significantly higher peaks occurring in measurements made near the Ohio River Valley, a region known for high industrial activity. The sensitivity studies performed in section 3.2.1, as well as GRASP retrievals, suggest that particle size is likely the primary driver of the differences in these two population, with the particles sampled over the Ohio River Valley being substantially smaller than urban aerosol sampled elsewhere. Despite the differences between these two classes of particles, the two types were combined into a single group due to underlying



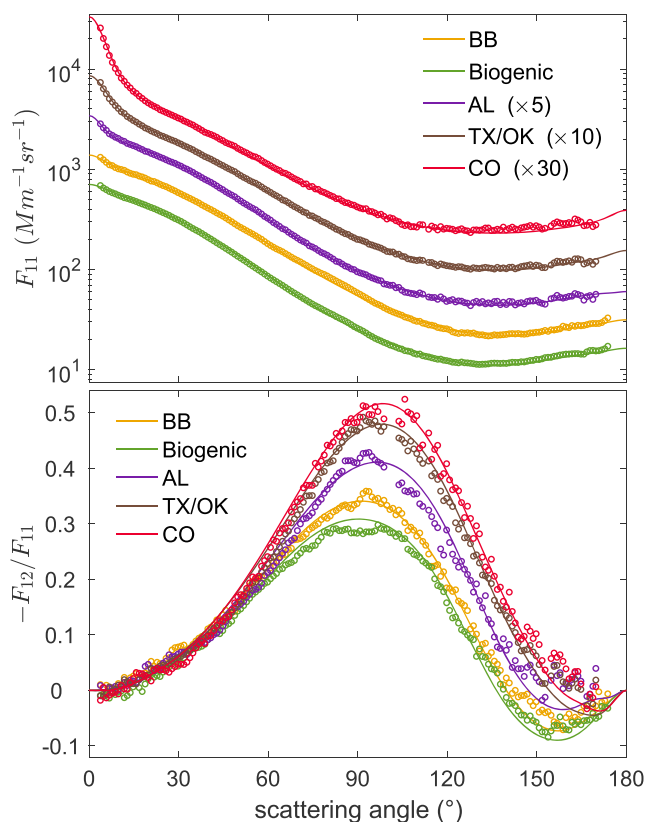


**Figure 6.** Mean measured scattering matrix elements (circles) and the corresponding GRASP fits (lines) for the five most prevalent aerosol types.

anthropogenic nature of the emissions and because the limited number of cases within each subtype prevented high-quality GRASP fits from being obtained. Additionally, the mean scattering matrix measurements and fits for the urban category were found to be almost identical to the biogenic data and were therefore omitted from Figure 6.

#### 4.1.3. Suitability of the Retrieval Assumptions

In order to retrieve properties of the aerosol from measurements containing limited information an inversion must make significant assumptions about the particles in question. In our application of the GRASP retrieval the two most significant assumptions are that the particles can be modeled by a combination of homogenous spheres and spheroids with a fixed shape distribution and that the refractive index is the same for all particles. In order to assess the retrieval's ability to reproduce the true optical properties of the sampled aerosol, we examine the residuals between the GRASP fits and PI-Neph measurements. These residuals are primarily driven by two distinct factors: (1) measurement errors in the PI-Neph data that cannot be fit by GRASP and (2) an inability of GRASP's aerosol model to produce the true angular scattering patterns produced by the sampled particles. In an attempt to isolate the contribution of the later factor, which is likely much smaller than the former factor, we have plotted in Figure 7 the median residuals of various aerosol types after the subtraction of the median residual of all samples from the corresponding campaign. The underlying assumption motivating the campaign wide median subtraction is that the contribution to the residuals that is driven by deficits in GRASP's aerosol assumptions will correlate significantly within but not between different particles types while systematic calibration errors present in PI-Neph data will be relatively constant across an entire campaign. The campaigns were treated separately as each of the two PI-Neph's had separate calibrations as well as instrument specific defects that lead to unique angularly dependent artifacts.

It should be emphasized that these adjusted residuals cannot be taken as absolute measures of the deficits of GRASP aerosol assumptions but merely provide upper bounds on the component of the fitting error that is specific to, and consistently observed, a single aerosol type. PI-Neph errors can also vary over time scales shorter than an entire campaign but long enough to persist in a type wide median, resulting in instrumental artifacts that remain in the adjusted residual plots. Factors contributing to these errors include long-term drifts in laser power, shifts in instrument alignment driving variations in stray light, and changes produced by contaminants settling on the optical elements. One tangible byproduct of these artifacts is the sharp transition of the SEAC<sup>4</sup>RS biomass burning  $-F_{12}/F_{11}$  adjusted residual around 90° in scattering angle. The PI-Neph illuminates the forward and backward angles with two partially independent laser beams, and these two regions therefore have unique calibration factors (Dolgos & Martins, 2014). High sensitivity in the  $-F_{12}/F_{11}$  measurement to errors in these two separate calibrations produced this observed sign change in the adjusted residuals around 90°. In SEAC<sup>4</sup>RS, this calibration drift seems to have happened to occur more severely in some types than others and, as a result, was not perfectly removed by the subtraction of the campaign wide median.

It is also possible that the overwhelming majority of samples from a given campaign share common features (e.g., unfavorable morphology and multiple particle types with very diverse refractive indices) that results in scattering patterns that GRASP is unable to reproduce. The residual signatures resulting from the inversions inability to fit these common features will be removed when the campaign wide median subtraction is performed. However, given the significant difference between each of these aerosol categories (Espinosa et al., 2018), it is unlikely that the fitting errors resulting from deficits in GRASP's assumptions would share significant commonalities. These plots therefore at least provide a qualitative picture of GRASP's remarkable ability to reproduce the true scattering properties of the particles. The fact that these adjusted residuals rarely

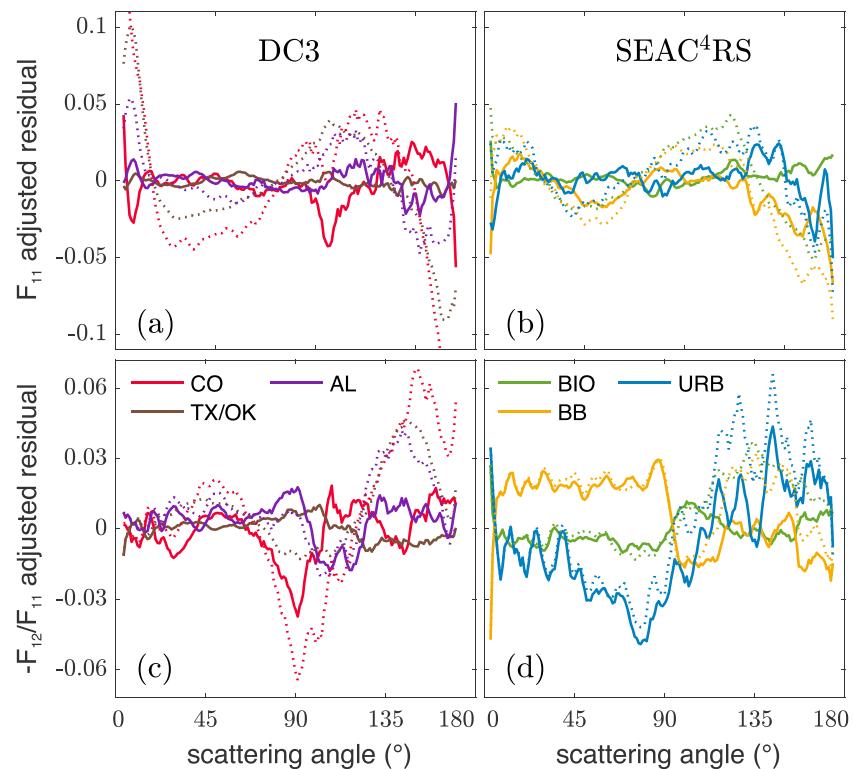


**Figure 7.** The adjusted residual between the 532-nm PI-Neph measurements and GRASP fits for each aerosol type. Panels (a) and (b) show the relative differences between the  $F_{11}$  fit and measurement for the DC3 and SEAC<sup>4</sup>RS aerosol types, respectively. Panels (c) and (d) show the absolute differences between the  $-F_{12}/F_{11}$  fit and measurement from the two field experiments. Within each panel the adjusted residuals of the standard retrieval (solid lines) are shown alongside the corresponding residuals obtained if the spheroid particles are not included in GRASP's aerosol assumptions (dotted line). The adjusted  $F_{11}$  residuals of the CO storm samples fit with only spheres extend beyond the vertical limits of panel (a) up to 0.2 and  $-0.2$  at the extreme forward and backward scattering angles, respectively.

extend beyond 2% speaks strongly to the capacity of the assumptions made within GRASP to accurately reproduce the true scattering patterns of a wide range of particle types.

In addition to the fits making use of spheres and spheroids shown in Figure 7 (solid lines), adjusted residuals resulting from the application of GRASP with only the use of spherical particles (dotted line) are also shown in Figure 7. This comparison allows us to investigate the benefits of incorporating the Dubovik et al. (2006) spheroid model over simply fitting with Mie theory alone. Significant biases appear in the sphere-only fits that are not present when the spheroid model is included. The limited ability of Mie theory alone to accurately reproduce the DC3  $F_{11}$  and  $-F_{12}/F_{11}$  data is particularly apparent. Additionally, the DC3 deviations can be seen to increase as the contribution of the likely nonspherical coarse mode increases, culminating in greater than 20% error in the case of the CO storm samples at the extreme forward and backward angles of  $F_{11}$  (plot cropped to enhance detail). This contrasts with a maximum of 5% fitting error in the same regions if the spheroid model is included in the fitting routine.

#### 4.2. Retrieved Aerosol Properties

After concluding that the GRASP retrievals are likely able to accurately reproduce the sampled optical properties, generally to within 2%, we examine GRASP retrievals of aerosol refractive index, size distribution, and spherical fraction. Overall, the retrieval results obtained in this work are generally found to agree well with the values presented in previous studies.

##### 4.2.1. Complex Refractive Indices

Measurements of dry aerosol refractive index are relatively rare, especially outside of laboratory measurements performed on artificially generated aerosols. Previous laboratory studies have deduced values of  $n$  in the visible that range from as low as 1.33 (the refractive index of pure water) to values greater than 1.6, with the differences being explained by different chemical compositions of the particles (Kim & Paulson, 2013). This wide range of values maps to a very diverse set of radiative properties in the corresponding aerosols.

Yu et al. (2012) found that the optical extinction produced by the fine mode of a typical naturally occurring aerosol could increase by a factor of two given a change in  $n$  from 1.33 to 1.53. It has also been demonstrated that a change in fine mode real refractive index of 0.1 can induce a change in the corresponding asymmetry parameters on the order of 10% (Kim et al., 2010). Moreover, the radiative properties tend to be even more sensitive to refractive index when coarse mode particles are included (Kim & Paulson, 2013). Redemann et al. (2000) showed that a 5% decrease in  $n$  can produce a decrease of around 30% in the radiative forcing at the top of the atmosphere given a realistic bimodal ambient aerosol. In the same study, it was also found that top of the atmosphere radiative forcing was less sensitive to the imaginary refractive index, with a 20% increase in  $k$  producing a 5% decrease in the radiative flux.

Field measurements of real refractive index have generally produced values falling within a slightly narrower range than their laboratory counterparts, suggesting that laboratory studies may be overestimating the variety of chemical compositions found in natural aerosols. Zhao (1999) also performed retrievals on polar nephelometer data and found a natural aerosol composed primarily of urban emissions in Sendai, Japan, to have a real refractive index of 1.52. The imaginary part of the refractive index was also retrieved and found to be on the order of 0.01, although the lack of a direct constraint on particle absorption led to a significant uncertainty in this parameter. Hand and Kreidenweis (2002) derived the real part of the refractive index for summertime aerosols over Texas, combining a Dynamic Mobility Analyzer (DMA) with an Optical Particle Counter (OPC), and obtained a value of 1.566. A DMA was also used, this time in combination with a polar nephelometer, by Dick et al. (2007) to retrieve a value of  $n = 1.49$  for aerosols located in the SEUS during July and August. Measurements made during DC3 and SEAC<sup>4</sup>RS by the Differential Aerosol Sizing and Hygroscopicity Spectrometer Probe (DASH-SP; Sorooshian et al., 2008) provided rarely obtained values of aerosol real refractive index above the surface layer (Aldhaif et al., 2018; Shingler et al., 2016; Sorooshian et al., 2017). The DASH-SP instrument also paired a DMA with an OPC to obtain values of  $n$  typically ranging from 1.5 to 1.54.

Box and whisker plots representing six of the parameters derived here from the retrievals of individual samples grouped by aerosol type are shown in Figure 8. The white central mark indicates the median value while the boxes denote the 25th and 75th percentiles with the whiskers extending to the 5th and 95th percentiles of the data. The real refractive indices retrieved from the sample averages of this study are shown in Table 4 and fall between 1.51 and 1.59 for all aerosol types. A modified version of the Monte Carlo simulation of section 3.3 was used to estimate the uncertainties of each of these retrieved parameters relative to the true mean value for that aerosol type.

In the modified uncertainty simulation the simulated instrumental errors corresponding to the individual samples were reduced to the values expected in the sample averages. The relative error of the PSAP data, which is expected to originate primarily from calibration and scattering correction uncertainties, was left at 20%, as these error sources are expected to correlate strongly across measurements of a single aerosol type. The simulated absolute error of the PSAP was reduced by the square root of the number of samples comprising the sample average as this error source is expected to originate primarily from photon counting noise for which no correlation between independent measurements is expected. The PI-Neph noise sources that are not expected to correlate between samples, which include photon counting noise and artifacts from insufficient particle statistics, were also reduced by the square root of the number of samples composing the type specific sample averages in the modified simulation. Several errors sources within the PI-Neph, primarily those driven by laser power variations and stray light inside the sample chamber, are expected to correlate on time scales on the order of an hour. Estimating the reduction in these uncertainties produced by averaging multiple samples is a more challenging task. In order to ensure that the error estimations derived from the Monte Carlo simulations do not underestimate the true errors, the simulated errors stemming from these sources have been reduced by the square root of the number of unique flight days composing the corresponding type. If every unique flight day of a given sample average contained the same number of individual samples, this procedure would represent errors that are completely correlated over a single flight day but completely uncorrelated from one day to the next, likely a significant over estimation of the true correlation times. These modified sample average Monte Carlo simulations containing the above error reductions were run with 3,000 iterations for each sample average, and the resulting RMSE values follow the “±” in Table 4.

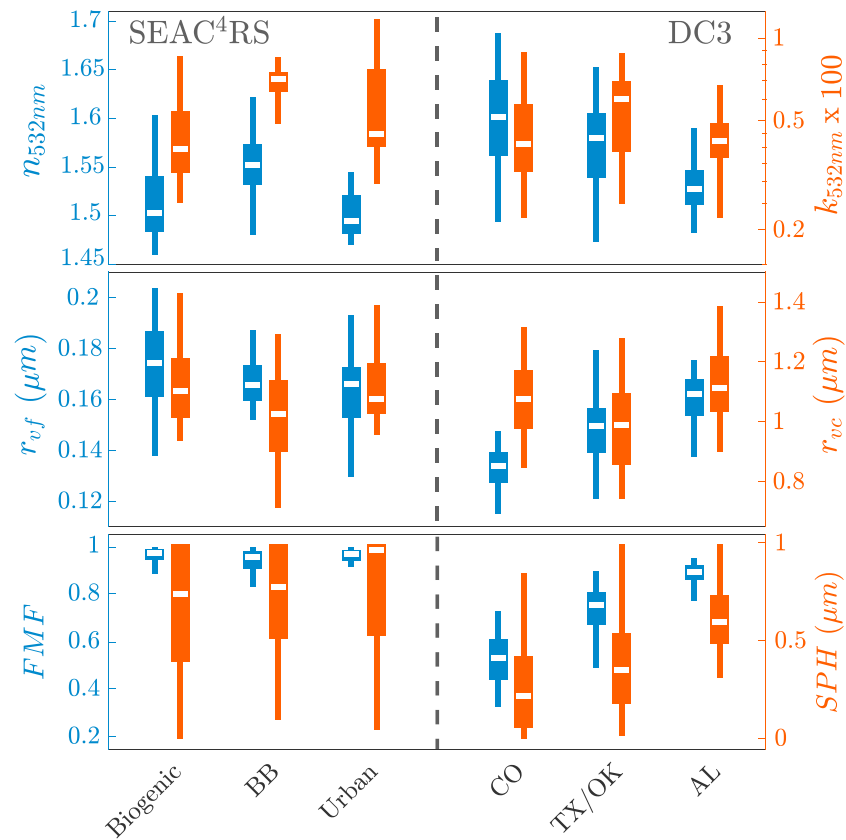


**Figure 8.** The spread of the retrieved complex refractive index, volume median radii, fine mode fraction, and spherical fraction values grouped by aerosol type. The white central mark indicates the median while the boxes denote the 25th and 75th percentiles with the whiskers extending to the 5th and 95th percentiles of the data.

It should be noted that the uncertainties in the values of Table 4 are driven primarily by systematic calibration errors since random errors with short correlation times are significantly reduced in the sample averages that are made up of many individual measurements. These errors are likely to be strongly correlated between aerosol types so the differences between types, especially within a single campaign, are more robust than the corresponding values themselves. For example, the differences in  $n$  on the order of 0.03–0.04 found between the BB and other SEAC<sup>4</sup>RS types is likely to be much more significant than the uncertainties ranging from 0.024–0.027 would imply if taken independently. This principle does not extend to the spectral dependence

**Table 4**  
*The Complex Refractive Indices and Spherical Fractions Retrieved From the Sample Averages of Each Aerosol Type Are Listed Along With the Corresponding 1σ Uncertainty Estimates Derived From the Monte Carlo Simulations*

Aerosol	SPH (%)	$n_{532nm}$	$k_{532nm} \times 100$	SSA
Biogenic	66 ± 23	1.51 ± 0.027	0.40 ± 0.09	0.977
BB	58 ± 19	1.55 ± 0.024	0.70 ± 0.16	0.962
Urban	85 ± 22	1.52 ± 0.026	0.50 ± 0.12	0.971
CO storms	17 ± 27	1.59 ± 0.057	0.43 ± 0.13	0.959
TX/OK storms	35 ± 28	1.56 ± 0.043	0.55 ± 0.13	0.962
AL storms	54 ± 33	1.52 ± 0.046	0.42 ± 0.12	0.973

*Note.* SPH = spherical particles. The single scattering albedo (SSA) retrieved from the sample averages are also shown for reference, although uncertainties were not estimated for derived parameters like SSA. The refractive indices and SSA values are all listed at 532 nm.

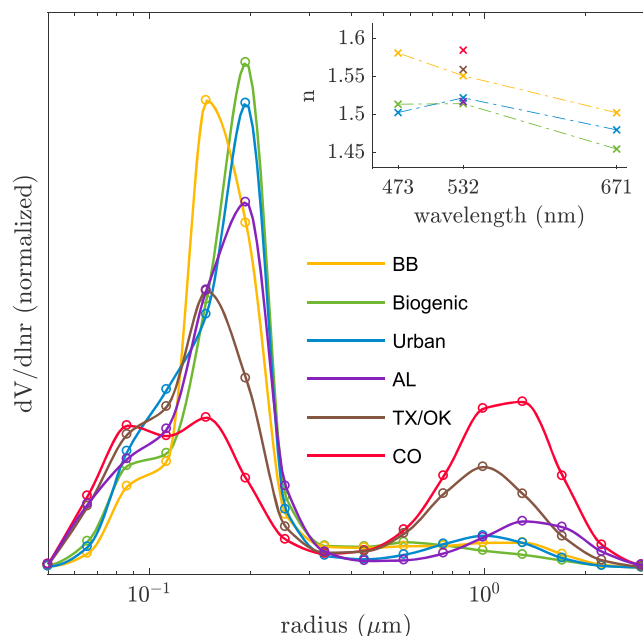


**Figure 9.** Normalized particle volume distributions and spectral real refractive indices (inset) retrieved from the sample averages of all explored classification types. Inlet cutoff effects, which predominately influence the largest particles, likely lead to an underestimation of the particle volume contained within the coarse mode.

derived for a given aerosol type as the three PI-Neph wavelengths are, for the most part, calibrated independently. Furthermore, the spectral slopes in real refractive index retrieved in this work are generally on the order of the inversion uncertainties and should therefore not be used to draw strong conclusions.

This elevated refractive index of the BB cases observed in the sample average retrievals, as well as in the individual sample inversion results portrayed in Figure 8, is a defining characteristic of the BB particles measured in this work. While the retrieval uncertainties are higher at 473 and 671 nm, the inset panel of Figure 9 shows that this elevated value of  $n$  also persists at these other two wavelengths. Espinosa et al. (2018) demonstrated that unique characteristics in the normalized angular scattering patterns of the BB samples allowed them to be correctly distinguished from the other SEAC<sup>4</sup>RS measurements in more than 90% of the cases. The parameters relating to size distribution are found to be remarkably similar (section 4.2.2), suggesting that the scattering differences, clearly evident between the two populations, may be driven primarily by differences in refractive index.

Measurements of dry BB real refractive indices are relatively rare, but several other studies have found higher values of  $n$  in BB particles than the values typically observed in other fine mode-dominated continental aerosols (Levin et al., 2010; Yamasoe et al., 1998). Additionally, the DASH-SP instrument retrieved an elevated real refractive index during SEAC<sup>4</sup>RS periods corresponding to wildfire emissions, although the representative value of 1.53–1.54 deduced by Shingler et al. (2016) is slightly lower than the values found in this study. This discrepancy may be partially explained by the fact that increased aerosol absorption, a feature also observed in the BB samples, can cause DASH-SP to underestimate the true real refractive index (Aldhaif et al., 2018). The elevated imaginary refractive index in these samples is likely driven by black carbon, which has a notably higher  $k$  value than other common particle constituents (Bergstrom et al., 2007; Kinne et al., 2003), and can be present in smoke aerosols in concentrations as high as 10% (Reid et al., 2005).

Corr et al. (2016) concluded, based on aerodynamic size distributions and chemical composition measurements, that a significant number of large dust particles were present in the air masses sampled by the DC-8 aircraft during DC3. Modeling studies have also shown that large convective systems can agitate surface soil particles, drawing these particles up into the atmosphere and acting as a significant source of dust aerosol (Seigel & van den Heever, 2012; Takemi et al., 2006). Dust aerosol often has a higher real refractive index than many of the other particles found over the study region (Curtis et al., 2008; Dubovik et al., 2002; Petzold et al., 2009); therefore, the elevated  $n_{532nm}$  values retrieved here from the DC3 measurements further support the hypothesis that significant quantities of dust-like particle were present. Furthermore, the differences in retrieved real refractive index between the storm domains may indicate differing quantities of dust among these three regions. The hypothesis that the CO storm domain had the largest proportion of dust particles, followed by the TX/OK and then AL domains, is further supported by the retrievals of particle size and morphology and will be discussed further in sections 4.2.2 and 4.2.3.

The measurements presented by Sorooshian et al. (2017), however, do not indicate increases in the the value of  $n$  when the DC-8 was sampling air associated with convective systems. These contradictory results can likely be explained by systemic differences in the particle populations sampled by the different instruments, with DASH-SP only measuring particles from the fine mode ( $90 \text{ nm} < r < 200 \text{ nm}$ ) while the PI-Neph and PSAP measured all particles small enough to pass through the aircraft inlet. If large dust particles were in fact driving the elevated refractive indices seen in the GRASP retrievals of PI-Neph and PSAP measurements, the effect would not be observed in the DASH-SP data, which is derived only from the fine mode particles.

**4.2.2. Particle Size Distributions**

Several trends are evident in the size distribution parameters retrieved from the individual samples, the statistics of which are also portrayed in Figure 8. The  $r_{vf}$  values are consistently skewed toward smaller particles in the DC3 retrievals relative to the corresponding SEAC<sup>4</sup>RS values. Furthermore, the Colorado storm

domain had consistently smaller fine mode particles than Alabama, with the Texas and Oklahoma domain falling between the two. No significant type-dependent differences were observed among the SEAC<sup>4</sup>RS  $r_{vf}$  values or any of the  $r_{vc}$  values. The size of the  $r_{vf}$  and  $r_{vc}$  whiskers are generally in line with what is expected given the uncertainties listed in Table 3 alone, suggesting limited variation in the true volume median radii within each type. The  $r_{vf}$  values obtained for biogenic and urban categories, however, did demonstrate more variability than could be explained by the retrieval uncertainty alone. No obvious  $r_{vf}$  correlations were found in the biogenic data, but two clear subgroups emerged within the urban samples. These two subgroups displayed strong spatial correlation, with the samples obtained near the Ohio River Valley containing smaller particles ( $\overline{r_{vf}} = 0.148 \mu\text{m}$ ) than the samples measured in close proximity to urban centers ( $\overline{r_{vf}} = 0.171 \mu\text{m}$ ).

All SEAC<sup>4</sup>RS fine mode fractions approach 100%, but a significant proportion of coarse mode particles were observed in the DC3 retrievals. The progression from CO to AL storms observed in the  $n_{532nm}$  and  $r_{vf}$  values is also seen in the distribution of retrieved FMF values. The variations in coarse mode particle concentrations among the three DC3 categories may be driven by increasingly arid surface features, leading to an increased availability of this relatively large dust aerosol (Tulet et al., 2010). In addition to the aridity of the underlying surface, variations in storm wind speeds may also have contributed to variations in the quantity of dust that was suspended over a given region.

The normalized size distributions retrieved from sample averages of each type are plotted in the main panel of Figure 9. The type-dependent differences in FMF observed in the individual sample retrievals shown in Figure 8 is also evident in these retrievals of the sample averages. The coarse modes shown in Figure 9 are all skewed toward smaller sizes relative to those retrieved by GRASP-like inversions applied to the total column ambient sky radiance measurements of AERONET (Dubovik et al., 2002). As mentioned in section 3.1.1, the inlet providing the sample flow to the PI-Neph onboard the DC-8 severely limited the transmission of coarser particles, truncating the upper end of the retrieved size distributions. While these inlet cutoff effects significantly influenced the coarse mode, fine mode particles properties are not expected to be meaningfully impacted (McNaughton et al., 2007).

The 16 bin PSD representation used by GRASP in this work allows the retrieval to reproduce a wide range of size distribution shapes. However, lower dimensional (e.g., lognormal) parameterizations are more easily transferred to other applications and are generally capable of reproducing their 16 bin counterparts with reasonable fidelity. The lognormal parameters calculated from the size distributions retrieved from the sample averages are shown in Table 5, along with their corresponding uncertainty estimates.

Several interesting features stand out in the parameterizations of the retrieved values. The intensive parameters representing the size distributions of the SEAC<sup>4</sup>RS types are again found to be remarkably similar, suggesting the difference observed in the corresponding scattering patterns are driven by deviations in other parameters, likely differences in refractive index. The values of  $r_{vf}$  in the three DC3 storm types further emphasizes that the aerosols in the vicinity of convective inflow had relatively small fine mode particles. A satisfactory physical explanation for this fact will require further study, but significant new particle formation, which often occurs in and around convective systems (Eck et al., 2014; Jeong & Li, 2010), may have played a role. This theory may be supported by the two adjacent fine mode peaks observed in the retrieval of the CO storms sample average, with the first peak potentially driven by fresh particles and the second peak being composed of older, larger fine mode aerosol. However, it is also possible that this PSD feature is an artifact produced by the specific GRASP size distribution constraints used in our retrievals and, therefore, is not a true characteristic of these particle populations. In future work, optimization of the retrieval setting may be able to reduce the likelihood of these types of artifacts.

Previous studies of comparable aerosols have often found dry fine mode size distributions that are slightly smaller than the values retrieved in this work. In their polar nephelometer retrievals Zhao (1999) also estimated the size of fine mode particles and found them to have a volume median radius of  $r_v = 0.11 \mu\text{m}$  with a relatively wide lognormal standard deviation of  $\sigma = 0.85$ . Kim et al. (1988) deduced a very similar average size distribution for aerosols over the non-summer time central United States, with a mean  $r_v$  also equal to  $0.11 \mu\text{m}$  and  $\sigma = 0.67$ . A variety of studies have found the fine mode volume median radius of BB emissions from temperate forests to be in the range  $0.1\text{--}0.15 \mu\text{m}$  (Reid et al., 2005). Analysis of speciated size distribution measurements made with a Laser Aerosol Spectrometer (LAS) OPC during SEAC<sup>4</sup>RS produced a BB size distribution very comparable to the size distributions retrieved by GRASP, with a LAS derived

**Table 5**

Parameterizations of the Fine and Coarse Mode Size Distributions Retrieved From the Sample Averages of Each Aerosol Type

Aerosol	$r_{vf}$ ( $\mu\text{m}$ )	$r_{vc}$ ( $\mu\text{m}$ )	$\sigma_f$	$\sigma_c$	$C_v$ ( $\frac{\mu\text{m}^3}{\text{cm}^3}$ )	$FMF$
Biogenic	$0.163 \pm 0.0063$	$0.87 \pm 0.11$	$0.36 \pm 0.05$	$0.40 \pm 0.04$	$13 \pm 1.0$	$0.93 \pm 0.015$
BB	$0.159 \pm 0.0049$	$0.97 \pm 0.11$	$0.32 \pm 0.04$	$0.40 \pm 0.03$	$24 \pm 1.6$	$0.91 \pm 0.015$
Urban	$0.155 \pm 0.0057$	$0.99 \pm 0.23$	$0.34 \pm 0.04$	$0.34 \pm 0.10$	$16 \pm 1.3$	$0.91 \pm 0.012$
CO Storms	$0.126 \pm 0.010$	$1.12 \pm 0.09$	$0.45 \pm 0.06$	$0.35 \pm 0.06$	$9.3 \pm 0.9$	$0.53 \pm 0.054$
TX/OK Storms	$0.138 \pm 0.0078$	$1.01 \pm 0.09$	$0.40 \pm 0.04$	$0.34 \pm 0.06$	$11 \pm 1.0$	$0.74 \pm 0.034$
AL Storms	$0.150 \pm 0.0099$	$1.30 \pm 0.21$	$0.38 \pm 0.06$	$0.37 \pm 0.06$	$11 \pm 1.3$	$0.87 \pm 0.038$

Note. The quantity following the  $\pm$  represents the  $1\sigma$  uncertainty in the corresponding values estimated from the Monte Carlo simulations. These uncertainties do not account for inlet cutoff effects, which likely cause the retrieved values of  $r_{vc}$ ,  $\sigma_c$ ,  $C_v$ , and  $FMF$  to differ significantly from the ambient values.

fine mode volume median radius on the order of  $0.16 \mu\text{m}$  (Shingler et al., 2016). However, the fine mode  $r_v$  values obtained by the LAS for other SEAC<sup>4</sup>RS particles types was generally lower ( $r_v \approx 0.11\mu\text{m}$ ) than the corresponding values obtained in this work. An analysis of LAS data obtained during DC3 was performed by Corr et al. (2016) and  $r_v \approx 0.11\mu\text{m}$  was also found to represent the bulk of these measurements.

A complete explanation as to why the  $r_{vf}$  values retrieved here are consistently larger than these other measurements is not fully apparent, but the inconsistency may at least partially stem from the frequent use of OPCs to determine aerosol size. OPCs measure the intensity of light scattered over a wide angular range by a single particle, which generally increases monotonically with particle size. The exact mapping between scattered light and aerosol size, however, depends significantly on the refractive index and morphology of the particles in question. In most cases these properties are not known exactly and the OPC is calibrated with a generic reference aerosol, polystyrene latex spheres ( $n_{532nm} > 1.6$ ; Jones et al., 2013) in the case of all of the aforementioned studies. The particles sampled during SEAC<sup>4</sup>RS and DC3 have been shown, in this work and others (Aldhaif et al., 2018), to have a consistently lower real refractive index than that of polystyrene and will therefore produce a weaker scattering signature in the LAS. Moreover, most OPC calibration standards, including polystyrene spheres, are nonabsorbing, which is not the case for many natural aerosols. The use of a reference aerosol, which overestimates  $n$  and underestimates  $k$ , will result in an OPC measurement that systematically underestimates the true geometric size of the particles.

The magnitude of the LAS biases can be estimated by examining the difference in scattering response over the LAS's angular range for different refractive indices of the aerosols. Using the response curves provided by Pinnick et al. (2000), it can be shown that a polystyrene particle with  $r = 0.15\mu\text{m}$  is optically equivalent (in terms of the scattering signal registered by the LAS instrument) to a dioctylphthalate ( $m_{633nm} = 1.485 + 0i$ ) particle that is  $0.015 \mu\text{m}$  smaller. In Espinosa et al. (2017) we examined a subset of 50 SEAC<sup>4</sup>RS measurements made by another OPC design, the Ultra-High Sensitivity Aerosol Spectrometer (UHSAS), and found that a calibration based on ammonium sulfate ( $m_{633nm} = 1.53 + 0i$ ) produced a size distribution with a volume median radius that was generally around  $0.025 \mu\text{m}$  larger than a calibration based on polystyrene spheres. Furthermore, the ammonium sulfate calibrated UHSAS data consistently produced size distributions that were skewed toward larger particles than GRASP retrievals of only PI-Neph data, with  $r_v \approx 0.175\mu\text{m}$  for the 50 selected SEAC<sup>4</sup>RS cases. In the present work, the magnitude of the deviation between the GRASP retrieved  $r_{vf}$  and corresponding value derived by the LAS is also consistent with the hypothesis that refractive index induced biases are driving a large part of the differences between the two techniques. The agreement between the two methods generally increases with the real refractive index, with higher values more closely matching the refractive index of polystyrene, as in the BB or CO storm cases. Moreover, potential LAS biases help to explain why Shingler et al. (2016) concluded, in opposition to the retrieval results of GRASP, that the BB category had significantly larger fine mode radii than the other particle types. The elevated refractive index observed in the SEAC<sup>4</sup>RS BB samples will produce larger scattering intensities for a fixed particle size, skewing the size distribution retrieved by the LAS to toward larger particles (Pinnick et al., 2000). This artifact in the LAS data emphasizes the need for well constrained refractive indices when making optical measurements of particle size, or ideally the simultaneous determination of size and refractive index.

### 4.2.3. Spherical Fractions

The spherical fractions retrieved from the sample averages cover a wide variety of values, ranging from almost no spherical particles in the Colorado storm domain ( $SPH = 17\%$ ) to a predominately spherical aerosol found in the urban retrieval ( $SPH = 85\%$ ). The reduced spherical fractions observed in the DC3 retrievals is another feature commonly observed in dust aerosol (Dubovik et al., 2006). Furthermore, the trends in these parameters mimic the trends observed in size distribution and refractive index, further suggesting that dust particles were most prevalent over the Colorado storm domain and second most prevalent over the Oklahoma and Texas domain.

The biogenic and urban categories were composed almost entirely of samples obtained over the summer time SEUS and had spherical fractions retrieved from the sample averages of 66% and 85%, respectively. These values compare relatively well with the results of Dick et al. (2007) who used azimuthal heterogeneity in light scattering to infer that around 90% of particles found in the summer time SEUS were spherical.

The morphology of BB particles can take on a variety of shapes including chain aggregates, solid irregulars and spheres, depending on the combustion material, burn conditions, and the time since emission (Reid et al., 2005). In the retrievals of SEAC<sup>4</sup>RS BB samples the scattering patterns were generally well reproduced by the spherical and spheroidal aerosol assumptions of GRASP. In Table 1 it can be seen that 99% of BB cases had  $F_{11}$  residuals that were less than 10% and the adjusted residuals of the BB cases, shown in Figure 7, were not significantly higher than the residuals for other types. Furthermore, the adjusted residuals do not increase significantly when only spherical particles are included, indicating that a spherical model alone can reproduce the optical properties of the sampled smoke well. These details however do not necessarily imply that the true BB particles were made up of geometric spheres. In fact, several studies have shown that the optical properties of a variety of smokes can correspond strongly with the expectations of spherical particles while Scanning Electron Microscope images reveal much more complex morphologies (Martins et al., 1998; Weiss et al., 1992). This result is not ubiquitous though, as at least one study has demonstrated that Mie scattering is inadequate to reproduce the scattering fields of some BB particles (Chakrabarty et al., 2007). It is possible that complex particle morphology may partially account for the elevated refractive index values of the BB samples, especially if these differences happen to closely mimic changes in  $n$  or  $k$  within the context of GRASP's aerosol assumptions.

## 5. Conclusions

In this work PI-Neph and PSAP measurements from the DC3 and SEAC<sup>4</sup>RS field experiments were sub-selected and averaged over periods corresponding to stable, high-quality data. An optically independent aerosol typing scheme, making use of ancillary data, was developed and the resulting 2,390 cases were separated into seven classified categories, as well as an eighth unclassified category corresponding to cases that did not meet any of the classification criteria. SEAC<sup>4</sup>RS measurements were separated into biogenic, BB, urban, and dust types, based on composition measurements from the PALMS instrument, APS data, and the concentrations of various gas tracers. The DC3 data set was divided into periods corresponding to the measurements from one of three storm domains located in Colorado, Texas, and Oklahoma as well as Alabama.

The GRASP retrieval, a generalized inversion technique to determine aerosol properties from optical measurements, was applied to the airborne measurements to obtain size distributions, complex refractive indices, and spherical fractions that are representative of each category. The addition of the PSAP data to the more established GRASP inversion of PI-Neph measurements represents, to our knowledge, the first combined retrieval of scattering matrix elements and filter-based absorption measurements. The retrieval results were examined with and without the inclusion of PSAP data and the extra constraint on absorption was found to significantly reduce the variability in the retrieved values of  $k$ . Furthermore, the incorporation of PSAP data caused a consistent decrease in the retrieved spherical fraction while simultaneously increasing the inverted real refractive index values. Monte Carlo simulations were performed to further explore the effects of including PSAP data, as well as better understand the retrieval uncertainties in general. In these simulations the inclusion of PSAP data produced significant increases in the accuracy of the retrieved  $k$ . Modest increases in the accuracy of the retrieved spherical fractions and real refractive indices were also observed, but parameters relating to PSD showed very slight decreases in accuracy. These conclusions generally held true even when our PSAP relative error estimate of 20% was doubled to 40%.



The aerosol assumptions present in GRASP generally proved sufficient to reproduce the observed scattering patterns with very high fidelity. A modified residual, designed to remove PI-Neph calibration errors, suggested that GRASP's assumptions permitted fitting of the scattering matrix elements to within 2% at the majority of angles. The removal of the spheroid component significantly degraded the quality of fits for many types, suggesting that Mie theory alone was not sufficient to reproduce the measured scattering patterns. When spheroids were included, over 80% of samples satisfied the condition, we imposed on the  $F_{11}$  fits requiring average residuals of less than 10%, with the bulk of the cases not satisfying the condition occurring at low aerosol loadings where the relative uncertainty of the PI-Neph is greatest. For reasons that are likely instrument specific, none of the GRASP retrievals of the samples in the dust category met the 10% residual condition, and the resulting retrieved parameters were therefore omitted from this work.

The retrieved refractive indices were generally in good agreement with the existing ranges from past studies. The inversions of the biogenic, urban, and AL storm categories all produced relatively small values of  $n_{532nm} \leq 1.52$ . The retrieved real refractive indices representative of the remaining types increased to 1.55, 1.56, and 1.59 in the BB, TX/OK and CO storm cases, respectively. Imaginary refractive indices were found to be in the very narrow range of  $0.004 \leq k_{532nm} \leq 0.005$ , with the exception of the TX/OK storm and BB types, which had  $k_{532nm}$  values of 0.0055 and 0.007, respectively.

The biogenic, urban, and BB types all had similar fine mode size distributions with volume median radii ranging from 0.155 to 0.163  $\mu\text{m}$  and  $0.32 \leq \sigma_f \leq 0.36$ . All three DC3 storm domains contained fine mode particles skewed toward smaller radii ( $r_{vf} \leq 0.15\mu\text{m}$ ) as well as significant quantities of coarse mode particles. The fine mode volume median radii retrieved in this work were often slightly higher than values determined in comparable studies. The bulk of these past studies have relied on measurements made by OPCs, and part of this discrepancy is potentially explained by differences in the real refractive indices retrieved here and those of the particles used in the OPC calibration. While coarse mode size distributions retrieved here provide qualitative information, the exact values are of less general interest and should not be used to derive remote sensing assumptions due to aerosol inlet cutoff effects strong influence on the larger particle sizes.

The distinct scattering properties consistently associated with the BB type were found to be explained, within the context of GRASP's aerosol assumptions, by an elevated real and imaginary refractive index. The magnitude of the scattering peak of  $-F_{12}/F_{11}$  was found to aid significantly in the discrimination of the BB type (Espinosa et al., 2018), and theoretical simulations performed here have shown this peak is particularly sensitive to refractive index. These facts support the conclusion of past studies (Mishchenko & Travis, 1997) that polarimetric remote sensing can significantly improve our ability to accurately distinguish different fine mode aerosols from space.

The retrieved size distributions, real refractive indices, and spherical fractions of the DC3 storms suggested a larger amount of dust in the CO samples than in the AL cases, with the TX/OK cases having dust concentrations laying somewhere between the other two domains. These trends in dust particles correlated closely with the aridity of the underlying surface features. Additionally, the skewing of the fine mode size distribution toward smaller particles may indicate new particle generation brought about by the convective systems.

## References

- Aldhaif, A. M., Stahl, C., Braun, R. A., Moghaddam, M. A., Shingler, T., Crosbie, E., et al. (2018). Characterization of the real part of dry aerosol refractive index over north america from the surface to 12 km. *Journal of Geophysical Research: Atmospheres*, *123*, 8283–8300. <https://doi.org/10.1029/2018JD028504>
- Anderson, T. L., Covert, D. S., Marshall, S. F., Laucks, M. L., Charlson, R. J., Waggoner, A. P., et al. (1996). Performance characteristics of a high-sensitivity, three-wavelength total scattering/backscatter nephelometer. *Journal of Atmospheric and Oceanic Technology*, *13*, 967–986.
- Barth, M. C., Cantrell, C. A., Brune, W. H., Rutledge, S. A., Crawford, J. H., Huntrieser, H., et al. (2015). The Deep Convective Clouds and Chemistry (DC3) field campaign. *Bulletin of the American Meteorological Society*, *96*(8), 1281–1309. <https://doi.org/10.1175/BAMS-D-13-00290.1>
- Bellouin, N., Boucher, O., Haywood, J., & Reddy, M. S. (2005). Global estimate of aerosol direct radiative forcing from satellite measurements. *Nature*, *438*(7071), 1138–1141.
- Bergstrom, R. W., Pilevskie, P., Russell, P. B., Redemann, J., Bond, T. C., Quinn, P. K., & Sierau, B. (2007). Spectral absorption properties of atmospheric aerosols. *Atmospheric Chemistry and Physics*, *7*(23), 5937–5943. <https://doi.org/10.5194/acp-7-5937-2007>
- Bilal, M., Nichol, J. E., Bleiweiss, M. P., & Dubois, D. (2013). A Simplified high resolution MODIS aerosol retrieval algorithm (SARA) for use over mixed surfaces. *Remote Sensing of Environment*, *136*, 135–145. <https://doi.org/10.1016/j.rse.2013.04.014>

## Acknowledgments

We acknowledge funding support from the NASA Earth Science Enterprise for the SEAC<sup>4</sup>RS campaign under Grant NNX12AC37G and under the Atmospheric Composition Campaign Data Analysis and Modeling Program (ACCDAM) Grant NNX14AP73G, both managed by Hal Maring. W. Reed Espinosa's participation in this research was partially supported by an appointment to the NASA Postdoctoral Program at the NASA Goddard Space Flight Center, administered by Universities Space Research Association through a contract with NASA. The authors would also like to thank the other members of the LARGE group, particularly Bruce Anderson and Andreas Beyersdorf for their support incorporating the PI-Neph into the LARGE instrument package. Moreover, we would like to thank the entire DC3 and SEAC<sup>4</sup>RS science teams for providing supporting data and relevant discussion. Lastly, we are grateful to the reviewers for their exceptionally constructive input. The GRASP software package is open-source and freely available for download at <http://www.grasp-open.com>. All relevant measurements made during the SEAC<sup>4</sup>RS experiment are available through the SEAC<sup>4</sup>RS data archive at <http://www-air.larc.nasa.gov/missions/seac4rs/> (SEAC<sup>4</sup>RS, 2013). The DC3 data set is also available through the corresponding archive, which can be found at <http://www-air.larc.nasa.gov/missions/dc3-seac4rs/> (DC3, 2012).

- Bond, T. C., Anderson, T. L., & Campbell, D. (1999). Calibration and intercomparison of filter-based measurements of visible light absorption by aerosols. *Aerosol Science & Technology*, 30(6), 582–600.
- Bond, T. C., Doherty, S. J., Fahey, D., Forster, P., Berntsen, T., DeAngelo, B., et al. (2013). Bounding the role of black carbon in the climate system: A scientific assessment. *Journal of Geophysical Research: Atmospheres*, 118, 5380–5552. <https://doi.org/10.1002/jgrd.50171>
- Chakrabarty, R. K., Moosmüller, H., Arnott, W. P., Garro, M. A., Slowik, J. G., Cross, E. S., et al. (2007). Light scattering and absorption by fractal-like carbonaceous chain aggregates: Comparison of theories and experiment. *Applied Optics*, 46(28), 6990–7006.
- Corr, C. A., Ziemba, L. D., Scheuer, E., Anderson, B. E., Beyersdorf, A. J., Chen, G., et al. (2016). Observational evidence for the convective transport of dust over the central United States. *Journal of Geophysical Research: Atmospheres*, 121, 1306–1319. <https://doi.org/10.1002/2015JD023789>
- Curtis, D. B., Meland, B., Aycibin, M., Arnold, N. P., Grassian, V. H., Young, M. A., & Kleiber, P. D. (2008). A laboratory investigation of light scattering from representative components of mineral dust aerosol at a wavelength of 550 nm. *Journal of Geophysical Research*, 113, D08210. <https://doi.org/10.1029/2007JD009387>
- DC3 (2012). Deep Convective Clouds and Chemistry experiment data archive. <https://doi.org/10.5067/Aircraft/DC3/DC8/Aerosol-TraceGas>
- Dick, W. D., Ziemann, P. J., & McMurry, P. H. (2007). Multiangle light-scattering measurements of refractive index of submicron atmospheric particles. *Aerosol Science and Technology*, 41(5), 549–569.
- Dolgos, G., & Martins, J. V. (2014). Polarized Imaging Nephelometer for in situ airborne measurements of aerosol light scattering. *Optics Express*, 22(18), 21,972–21,990. <https://doi.org/10.1364/OE.22.021972>
- Dubovik, O. (2004). Optimization of Numerical Inversion in Photopolarimetric Remote Sensing. *Photopolarimetry in Remote Sensing*, pp. 65–106. [https://doi.org/10.1007/1-4020-2368-5\\_3](https://doi.org/10.1007/1-4020-2368-5_3)
- Dubovik, O., Herman, M., Holdak, a., Lapyonok, T., Tanré, D., Deuzé, J. L., et al. (2011). Statistically optimized inversion algorithm for enhanced retrieval of aerosol properties from spectral multi-angle polarimetric satellite observations. *Atmospheric Measurement Techniques*, 4(5), 975–1018. <https://doi.org/10.5194/amt-4-975-2011>
- Dubovik, O., Holben, B., Eck, T., Smirnov, A., Kaufman, Y., & King, M. (2002). Variability of absorption and optical properties of key aerosol types observed in worldwide locations. *Journal of the Atmospheric Sciences*, 59, 590–608.
- Dubovik, O., Lapyonok, T., Litvinov, P., Herman, M., Fuertes, D., Ducos, F., et al. (2014). GRASP: A versatile algorithm for characterizing the atmosphere. *SPIE Newsroom* 2–5, <https://doi.org/10.1117/2.1201408.005558>
- Dubovik, O., Sinyuk, A., Lapyonok, T., Holben, B. N., Mishchenko, M., Yang, P., et al. (2006). Application of spheroid models to account for aerosol particle nonsphericity in remote sensing of desert dust. *Journal of Geophysical Research*, 111, D11208. <https://doi.org/10.1029/2005JD006619>
- Dubovik, O., Smirnov, a., Holben, B. N., King, M. D., Kaufman, Y. J., Eck, T. F., & Slutsker, I. (2000). Accuracy assessments of aerosol optical properties retrieved from Aerosol Robotic Network (AERONET) Sun and sky radiance measurements. *Journal of Geophysical Research*, 105(D8), 9791–9806. <https://doi.org/10.1029/2000JD900040>
- Eck, T. F., Holben, B. N., Reid, J. S., Arola, A., Ferrare, R. A., Hostetler, C. A., et al. (2014). Observations of rapid aerosol optical depth enhancements in the vicinity of polluted cumulus clouds. *Atmospheric Chemistry and Physics*, 14(21), 11,633–11,656. <https://doi.org/10.5194/acp-14-11633-2014>
- Espinosa, W. R., Martins, J. V., Remer, L. A., Puthukkudy, A., Orozco, D., & Dolgos, G. (2018). In situ measurements of angular-dependent light scattering by aerosols over the contiguous United States. *Atmospheric Chemistry and Physics*, 18(5), 3737–3754. <https://doi.org/10.5194/acp-18-3737-2018>
- Espinosa, W. R., Remer, L. A., Dubovik, O., Ziemba, L., Beyersdorf, A., Orozco, D., et al. (2017). Retrievals of aerosol optical and microphysical properties from imaging polar nephelometer scattering measurements. *Atmospheric Measurement Techniques*, 10(3), 811. <https://doi.org/10.5194/amt-10-811-2017>
- Fedarenka, A., Dubovik, O., Goloub, P., Li, Z., Lapyonok, T., Litvinov, P., et al. (2016). Utilization of AERONET polarimetric measurements for improving retrieval of aerosol microphysics: GSFC, Beijing and Dakar data analysis. *Journal of Quantitative Spectroscopy and Radiative Transfer*, 179, 72–97.
- Fried, A., Diskin, G., Weibring, P., Richter, D., Walega, J., Sachse, G., et al. (2008). Tunable infrared laser instruments for airborne atmospheric studies. *Applied Physics B*, 92(3), 409–417.
- Gakidou, E., Afshin, A., Abajobir, A. A., Abate, K. H., Abbafati, C., Abbas, K. M., et al. (2017). Global, regional, and national comparative risk assessment of 84 behavioural, environmental and occupational, and metabolic risks or clusters of risks, 1990–2016: A systematic analysis for the Global Burden of Disease Study 2016. *The Lancet*, 390(10100), 1345–1422.
- Goldstein, A. H., Koven, C. D., Heald, C. L., & Fung, I. Y. (2009). Biogenic carbon and anthropogenic pollutants combine to form a cooling haze over the southeastern United States. *Proceedings of the National Academy of Sciences*, 106(22), 8835–8840.
- Hand, J. L., & Kreidenweis, S. M. (2002). A new method for retrieving particle refractive index and effective density from aerosol size distribution data. *Aerosol Science and Technology*, 36(10), 1012–1026. <https://doi.org/10.1080/02786820290092276>
- Holben, B., Eck, T., Slutsker, I., & Tanre, D. (1998). AERONET federated instrument network and data archive for aerosol characterization. *Remote Sensing of the Environment*, 4257(98), 1–16.
- Jeong, M.-J., & Li, Z. (2010). Separating real and apparent effects of cloud, humidity, and dynamics on aerosol optical thickness near cloud edges. *Journal of Geophysical Research*, 115, D00K32. <https://doi.org/10.1029/2009JD013547>
- Jones, S. H., King, M. D., & Ward, A. D. (2013). Determining the unique refractive index properties of solid polystyrene aerosol using broadband Mie scattering from optically trapped beads. *Physical Chemistry Chemical Physics*, 15(47), 20735. <https://doi.org/10.1039/c3cp53498g>
- Kim, H., Barkey, B., & Paulson, S. E. (2010). Real refractive indices of  $\alpha$ - and  $\beta$ -pinene and toluene secondary organic aerosols generated from ozonolysis and photo-oxidation. *Journal of Geophysical Research*, 115, D24212. <https://doi.org/10.1029/2010JD014549>
- Kim, H., & Paulson, S. E. (2013). Real refractive indices and volatility of secondary organic aerosol generated from photooxidation and ozonolysis of limonene,  $\alpha$ -pinene and toluene. *Atmospheric Chemistry and Physics*, 13(15), 7711–7723.
- Kim, Y. J., Sievering, H., & Boatman, J. (1988). Airborne measurement of atmospheric aerosol particles in the lower troposphere over the central United States. *Journal of Geophysical Research*, 93(D10), 12,631–12,644.
- Kinne, S., Lohmann, U., Feichter, J., Schulz, M., Timmreck, C., Ghan, S., et al. (2003). Monthly averages of aerosol properties: A global comparison among models, satellite data, and AERONET ground data. *Journal of Geophysical Research*, 108(D20), 4634. <https://doi.org/10.1029/2001JD001253>
- Lee, J., Kim, J., Yang, P., & Hsu, N. C. (2012). Improvement of aerosol optical depth retrieval from MODIS spectral reflectance over the global ocean using new aerosol models archived from AERONET inversion data and tri-axial ellipsoidal dust database. *Atmospheric Chemistry and Physics*, 12(15), 7087–7102. <https://doi.org/10.5194/acp-12-7087-2012>

- Levin, E., McMeeking, G., Carrico, C., Mack, L., Kreidenweis, S., Wold, C., et al. (2010). Biomass burning smoke aerosol properties measured during fire laboratory at Missoula experiments (flame). *Journal of Geophysical Research*, *115*, D18210. <https://doi.org/10.1029/2009JD013601>
- Levy, R. C., Remer, L. A., & Dubovik, O. (2007). Global aerosol optical properties and application to Moderate Resolution Imaging Spectroradiometer aerosol retrieval over land. *Journal of Geophysical Research*, *112*, D13210. <https://doi.org/10.1029/2006JD007815>
- Li, Z., Goloub, P., Dubovik, O., Blarel, L., Zhang, W., Podvin, T., et al. (2009). Improvements for ground-based remote sensing of atmospheric aerosol properties by additional polarimetric measurements. *Journal of Quantitative Spectroscopy and Radiative Transfer*, *110*(17), 1954–1961.
- Malm, W. C., Schichtel, B. A., Pitchford, M. L., Ashbaugh, L. L., & Eldred, R. A. (2004). Spatial and monthly trends in speciated fine particle concentration in the United States. *Journal of Geophysical Research*, *109*, D03306. <https://doi.org/10.1029/2003JD003739>
- Martins, J. V., Hobbs, P. V., Weiss, R. E., & Artaxo, P. (1998). Sphericity and morphology of smoke particles from biomass burning in Brazil. *Journal of Geophysical Research*, *103*(D24), 32,051–32,057. <https://doi.org/10.1029/98JD01153>
- Mason, B., Wagner, N., Adler, G., Andrews, E., Brock, C., Gordon, T., et al. (2018). An intercomparison of aerosol absorption measurements conducted during the SEAC4RS campaign. *Aerosol Science and Technology*, *52*(9), 1012–1027.
- McNaughton, C. S., Clarke, A. D., Howell, S. G., Pinkerton, M., Anderson, B., Thornhill, L., et al. (2007). Results from the DC-8 Inlet Characterization Experiment (DICE): Airborne versus surface sampling of mineral dust and sea salt aerosols. *Aerosol Science and Technology*, *41*(2), 136–159. <https://doi.org/10.1080/02786820601118406>
- Mikoviny, T., Kaser, L., & Wisthaler, A. (2010). Development and characterization of a high-temperature proton-transfer-reaction mass spectrometer (HT-PTR-MS). *Atmospheric Measurement Techniques*, *3*(3), 537–544.
- Mishchenko, M. I., Dlugach, J. M., & Liu, L. (2016). Applicability of the effective-medium approximation to heterogeneous aerosol particles. *Journal of Quantitative Spectroscopy and Radiative Transfer*, *178*, 284–294.
- Mishchenko, M. I., & Travis, L. D. (1997). Satellite retrieval of aerosol properties over the ocean using polarization as well as intensity of reflected sunlight. *Journal of Geophysical Research*, *102*(D14), 16,989–17,013. <https://doi.org/10.1029/96JD02425>
- Mishchenko, M. I., Travis, L. D., & Lacis, A. A. (2002). *Scattering, absorption, and emission of light by small particles*. Cambridge, UK: Cambridge University Press.
- Müller, T., Henzing, J. S., de Leeuw, G., Wiedensohler, A., Alastuey, A., Angelov, H., et al. (2011). Characterization and intercomparison of aerosol absorption photometers: result of two intercomparison workshops. *Atmospheric Measurement Techniques*, *4*(2), 245–268. <https://doi.org/10.5194/amt-4-245-2011>
- Myhre, G., Samsset, B., Schulz, M., Balkanski, Y., Bauer, S., Berntsen, T., et al. (2013). Radiative forcing of the direct aerosol effect from aerosol phase II simulations. *Atmospheric Chemistry and Physics*, *13*(4), 1853.
- Peterson, D. A., Hyer, E. J., Campbell, J. R., Fromm, M. D., Hair, J. W., Butler, C. F., & Fenn, M. A. (2015). The 2013 rim fire: Implications for predicting extreme fire spread, pyroconvection, and smoke emissions. *Bulletin of the American Meteorological Society*, *96*(2), 229–247.
- Petzold, A., Rasp, K., Weinzierl, B., Esselborn, M., Hamburger, T., & Dörnbrack, A. (2009). Saharan dust absorption and refractive index from aircraft-based observations during SAMUM 2006. *Tellus B*, *61*(1), 118–130. <https://doi.org/10.1111/j.1600-0889.2008.00383.x>
- Pinnick, R. G., Pendleton, J., & Videen, G. (2000). Response characteristics of the particle measuring systems active scattering aerosol spectrometer probes. *Aerosol Science & Technology*, *33*(4), 334–352.
- Pollack, I. B., Lerner, B. M., & Ryerson, T. B. (2010). Evaluation of ultraviolet light-emitting diodes for detection of atmospheric NO<sub>2</sub> by photolysis-chemiluminescence. *Journal of Atmospheric Chemistry*, *65*(2), 111–125. <https://doi.org/10.1007/s10874-011-9184-3>
- Redemann, J., Turco, R., Liou, K., Hobbs, P., Hartley, W., Bergstrom, R., et al. (2000). Case studies of the vertical structure of the direct shortwave aerosol radiative forcing during TARFOX. *Journal of Geophysical Research*, *105*(D8), 9971–9979. <https://doi.org/10.1029/1999JD901042>
- Reid, J., Koppmann, R., Eck, T., & Eleuterio, D. (2005). A review of biomass burning emissions part II: intensive physical properties of biomass burning particles. *Atmospheric Chemistry and Physics*, *5*(3), 799–825.
- Rosenfeld, D., Lohmann, U., Raga, G. B., O'Dowd, C. D., Kulmala, M., Fuzzi, S., et al. (2008). Flood or drought: How do aerosols affect precipitation? *Science*, *321*(5894), 1309–1313.
- Russell, P. B., Livingston, J. M., Dubovik, O., Ramirez, S. A., Wang, J., Redemann, J., et al. (2004). Sunlight transmission through desert dust and marine aerosols: Diffuse light corrections to sun photometry and pyrrometry. *Journal of Geophysical Research*, *109*, D08207. <https://doi.org/10.1029/2003JD004292>
- Ryerson, T. B., Williams, E. J., & Fehsenfeld, F. C. (2000). An efficient photolysis system for fast-response NO<sub>2</sub> measurements. *Journal of Geophysical Research*, *105*(D21), 26,447–26,461. <https://doi.org/10.1029/2000JD900389>
- SEAC4RS (2013). Studies of emissions and atmospheric composition. Clouds and Climate Coupling by Regional Surveys Data Archive, <https://doi.org/10.5067/Aircraft/SEAC4RS/Aerosol-TraceGas-Cloud>
- Schafer, J. S., Eck, T. F., Holben, B. N., Thornhill, K. L., Anderson, B. E., Sinyuk, A., et al. (2014). Intercomparison of aerosol single-scattering albedo derived from AERONET surface radiometers and large in situ aircraft profiles during the 2011 DRAGON-MD and DISCOVER-AQ experiments. *Journal of Geophysical Research: Atmospheres*, *119*, 7439–7452. <https://doi.org/10.1002/2013JD021166>
- Schmid, O., Artaxo, P., Arnott, W., Chand, D., Gatti, L. V., Frank, G., et al. (2006). Spectral light absorption by ambient aerosols influenced by biomass burning in the Amazon basin. I: Comparison and field calibration of absorption measurement techniques. *Atmospheric Chemistry and Physics*, *6*(11), 3443–3462.
- Schulz, M., Textor, C., Kinne, S., Balkanski, Y., Bauer, S., Berntsen, T., et al. (2006). Radiative forcing by aerosols as derived from the aerosol present-day and pre-industrial simulations. *Atmospheric Chemistry and Physics*, *6*(12), 5225–5246.
- Seigel, R. B., & van den Heever, S. C. (2012). Dust lofting and ingestion by supercell storms. *Journal of the Atmospheric Sciences*, *69*(5), 1453–1473.
- Shingler, T., Crosbie, E., Ortega, A., Shiraiwa, M., Zuend, A., Beyersdorf, A., et al. (2016). Airborne characterization of subsaturated aerosol hygroscopicity and dry refractive index from the surface to 6.5 km during the SEAC4RS campaign. *Journal of Geophysical Research: Atmospheres*, *121*, 4188–4210. <https://doi.org/10.1002/2015JD024498>
- Sorooshian, A., Hersey, S., Brechtel, F. J., Corless, A., Flagan, R. C., & Seinfeld, J. H. (2008). Rapid, size-resolved aerosol hygroscopic growth measurements: Differential aerosol sizing and hygroscopicity spectrometer probe (DASH-SP). *Aerosol Science and Technology*, *42*(6), 445–464.
- Sorooshian, A., Shingler, T., Crosbie, E., Barth, M., Homeyer, C., Campuzano-Jost, P., et al. (2017). Contrasting aerosol refractive index and hygroscopicity in the inflow and outflow of deep convective storms: Analysis of airborne data from DC3. *Journal of Geophysical Research: Atmospheres*, *122*, 4565–4577. <https://doi.org/10.1002/2017JD026638>
- Stein, A., Draxler, R. R., Rolph, G. D., Stunder, B. J., Cohen, M., & Ngan, F. (2015). NOAA's HYSPLIT atmospheric transport and dispersion modeling system. *Bulletin of the American Meteorological Society*, *96*(12), 2059–2077.

- Stocker, T. (2014). *Climate change 2013: the physical science basis: Working Group I contribution to the fifth assessment report of the Intergovernmental Panel on Climate Change*. Cambridge University Press.
- Takemi, T., Yasui, M., Zhou, J., & Liu, L. (2006). Role of boundary layer and cumulus convection on dust emission and transport over a midlatitude desert area. *Journal of Geophysical Research*, *111*, 2156–2202. <https://doi.org/10.1029/2005JD006666>
- Tanré, D., Kaufman, Y., Herman, M., & Mattoo, S. (1997). Remote sensing of aerosol properties over oceans using the MODIS/EOS spectral radiances. *Journal of Geophysical Research*, *102*(D14), 16,971–16,988. <https://doi.org/10.1029/96JD03437>
- Thomson, D. S., Schein, M. E., & Murphy, D. M. (2000). Particle analysis by laser mass spectrometry WB-57F instrument overview. *Aerosol Science & Technology*, *33*(1-2), 153–169.
- Toon, O. B., Maring, H., Dibb, J., Ferrare, R., Jacob, D. J., Jensen, E. J., et al. (2016). Planning, implementation and scientific goals of the Studies of Emissions and Atmospheric Composition, Clouds and Climate Coupling by Regional Surveys (SEAC4RS) field mission. *Journal of Geophysical Research: Atmospheres*, *121*, 4967–5009. <https://doi.org/10.1002/2015JD024297>
- Tulet, P., Crahan-Kaku, K., Leriche, M., Aouizerats, B., & Crumeyrolle, S. (2010). Mixing of dust aerosols into a mesoscale convective system. *Atmospheric Research: 15th International Conference on Clouds and Precipitation.*, *96*(2), 302–314. <https://doi.org/10.1016/j.atmosres.2009.09.011>
- Van Donkelaar, A., Martin, R. V., & Park, R. J. (2006). Estimating ground-level PM<sub>2.5</sub> using aerosol optical depth determined from satellite remote sensing. *Journal of Geophysical Research*, *111*, D21201. <https://doi.org/10.1029/2005JD006996>
- Virkkula, A. (2010). Correction of the calibration of the 3-wavelength particle soot absorption photometer (3λ PSAP). *Aerosol Science and Technology*, *44*(8), 706–712.
- Virkkula, A., Ahlquist, N. C., Covert, D. S., Arnott, W. P., Sheridan, P. J., Quinn, P. K., & Coffman, D. J. (2005). Modification, calibration and a field test of an instrument for measuring light absorption by particles. *Aerosol Science and Technology*, *39*(1), 68–83.
- Volten, H., Munoz, O., Rol, E., Haan, J. V. W., & Hovenier, J. (2001). Scattering matrices of mineral aerosol particles at 441.6 nm and 632.8 nm. *Journal of Geophysical Research*, *106*(D115), 17,375–17,401. <https://doi.org/10.1029/2001JD900068>
- Wang, J., & Christopher, S. A. (2003). Intercomparison between satellite-derived aerosol optical thickness and PM<sub>2.5</sub> mass: Implications for air quality studies. *Geophysical research letters*, *30*(21), 2095. <https://doi.org/10.1029/2003GL018174>
- Weiss, R. E., Kapustin, V. N., & Hobbs, P. V. (1992). Chain-aggregate aerosols in smoke from the Kuwait oil fires. *Journal of Geophysical Research*, *97*(D13), 14,527–14,531. <https://doi.org/10.1029/92JD01372>
- Wong, M. S., Nichol, J. E., & Lee, K. H. (2011). An operational MODIS aerosol retrieval algorithm at high spatial resolution, and its application over a complex urban region. *Atmospheric Research*, *99*(3-4), 579–589. <https://doi.org/10.1016/j.atmosres.2010.12.015>
- Yamasoe, M. a., Kaufman, Y. J., Dubovik, O., Remer, L. a., Holben, B. N., & Artaxo, P. (1998). Retrieval of the real part of the refractive index of smoke particles from Sun/sky measurements during SCAR-B. *Journal of Geophysical Research*, *103*(98), 31,893–31,902. <https://doi.org/10.1029/98JD01211>
- Young, A. T. (1980). Revised depolarization corrections for atmospheric extinction. *Applied optics*, *19*(20), 3427–3428.
- Yu, F., Luo, G., & Ma, X. (2012). Regional and global modeling of aerosol optical properties with a size, composition, and mixing state resolved particle microphysics model. *Atmospheric Chemistry and Physics*, *12*(13), 5719–5736.
- Zhao, F. (1999). Determination of the complex index of refraction and size distribution of aerosols from polar nephelometer measurements. *Applied optics*, *38*(12), 2331–2336.
- Zhao, F., Gong, Z., Hu, H., Tanaka, M., & Hayasaka, T. (1997). Simultaneous determination of the aerosol complex index of refraction and size distribution from scattering measurements of polarized light. *Applied optics*, *36*(30), 7992–8001.
- Ziemba, L. D., Beyersdorf, A. J., Chen, G., Corr, C. A., Crumeyrolle, S. N., Diskin, G., et al. (2016). Airborne observations of bioaerosol over the southeast United States using a wideband integrated bioaerosol sensor. *Journal of Geophysical Research: Atmospheres*, *121*, 8506–8524. <https://doi.org/10.1002/2015JD024669>